Seismic anisotropy and its precursory change before eruptions at Piton de la Fournaise volcano, La Réunion

M. K. Savage, V. Ferrazzini, Aline Peltier, E. Rivemale, J. Mayor, A. Schmid, F. Brenguier, F. Massin, J. Got, J. Battaglia, et al.

RESEARCH ARTICLE

Key Points:
- Average fast directions are radial to the central crater
- Vp/Vs ratios suggest regions of fluid- or gas-filled cracks
- Magmatic pressure changes and fluid movement cause variations in splitting

Seismic anisotropy and its precursory change before eruptions at Piton de la Fournaise volcano, La Réunion

M. K. Savage[1], V. Ferrazzini[2], A. Peltier[2], E. Rivemale[3], J. Mayor[4], A. Schmid[3], F. Brenguier[3], F. Massin[5], J.-L. Got[3], J. Battaglia[6], A. DiMuro[2], T. Staudacher[2], D. Rivet[7], B. Taisne[8], and A. Shelley[1]

[1]Institute of Geophysics, Victoria University of Wellington, Wellington, New Zealand, [2]Observatoire Volcanologique du Piton de la Fournaise, Institut de Physique du Globe de Paris, CNRS, UMR 7154–Géologie des Systèmes Volcaniques, Réunion, France, [3]Institut des Sciences de la Terre, Université de Grenoble, Grenoble, France, [4]Institut de Recherche en Astrophysique et Planétologie, CNRS, Université Toulouse III, [5]Observatoire Volcanologique et Sismologique de Martinique (IPGP), Fonds St. Denis, Martinique, [6]Laboratoire Magmas et Volcans, CNRS, Université Blaise Pascal, IRD, Clermont-Ferrand, France, [7]GeoAzur, University of Nice Sophia-Antipolis, Côte d'Azur Observatory, CNRS, Sophia Antipolis, France, [8]Earth Observatory of Singapore, Nanyang Technological University, Singapore

Abstract The Piton de la Fournaise volcano exhibits frequent eruptions preceded by seismic swarms and is a good target to test hypotheses about magmatically induced variations in seismic wave properties. We use a permanent station network and a portable broadband network to compare seismic anisotropy measured via shear wave splitting with geodetic displacements, ratios of compressional to shear velocity (Vp/Vs), earthquake focal mechanisms, and ambient noise correlation analysis of surface wave velocities and to examine velocity and stress changes from 2000 through 2012. Fast directions align radially to the central cone and parallel to surface cracks and fissures, suggesting stress-controlled cracks. High Vp/Vs ratios under the summit compared with low ratios under the flank suggest spatial variations in the proportion of fluid-filled versus gas-filled cracks. Secular variations of fast directions (ϕ) and delay times (dt) between split shear waves are interpreted to sense changing crack densities and pressure. Delay times tend to increase while surface wave velocity decreases before eruptions. Rotations of ϕ may be caused by changes in either stress direction or fluid pressure. These changes usually correlate with GPS baseline changes. Changes in shear wave splitting measurements made on multiplets yield several populations with characteristic delay times, measured incoming polarizations, and fast directions, which change their proportion as a function of time. An eruption sequence on 14 October 2010 yielded over 2000 shear wave splitting measurements in a 14 h period, allowing high time resolution measurements to characterize the sequence. Stress directions from a propagating dike model qualitatively fit the temporal change in splitting.

1. Introduction

Identifying precursory changes in seismic properties before earthquakes and volcanic eruptions has long been a goal of seismologists. Several recent studies have separately proposed changes in isotropic seismic velocity [e.g., *Brenguier et al.*, 2008] or anisotropy [*Bianco et al.*, 2006; *Gerst and Savage*, 2004; *Savage et al.*, 2010b] prior to eruptions. The interpretation of these studies was that the spatial distribution and orientation of cracks were changed by the action of the stress field before eruptions. At the Piton de la Fournaise (PdF) volcano, we compare these techniques directly to each other, as well as to geodetic measures of displacement on the volcano, earthquake fault plane solutions, and Vp/Vs ratios, in order to investigate the mechanisms responsible for the changes.

Care must be taken to ensure that temporal variations in earthquake locations are not mistakenly considered to be changes in path properties. In addition, multiple layers of anisotropy can cause large variations in shear wave splitting parameters as a function of the incoming polarization direction (ϕ_{in}) [*Silver and Savage*, 1994]. For local earthquakes, ϕ_{in} is determined by the fault orientation and ray propagation direction. To minimize these effects, we use earthquake "multiplets," that is, groups of events with similar waveform, which are considered to have occurred within a few tens of meters of each other (one-fourth wavelength) and with almost identical focal mechanisms [*Geller and Mueller*, 1980].

1.1. Regional Tectonics

The Piton de la Fournaise volcano (PdF) is an active basaltic volcano on the island of La Réunion in the Indian Ocean, which has been monitored geophysically and geochemically by the Volcanological Observatory of
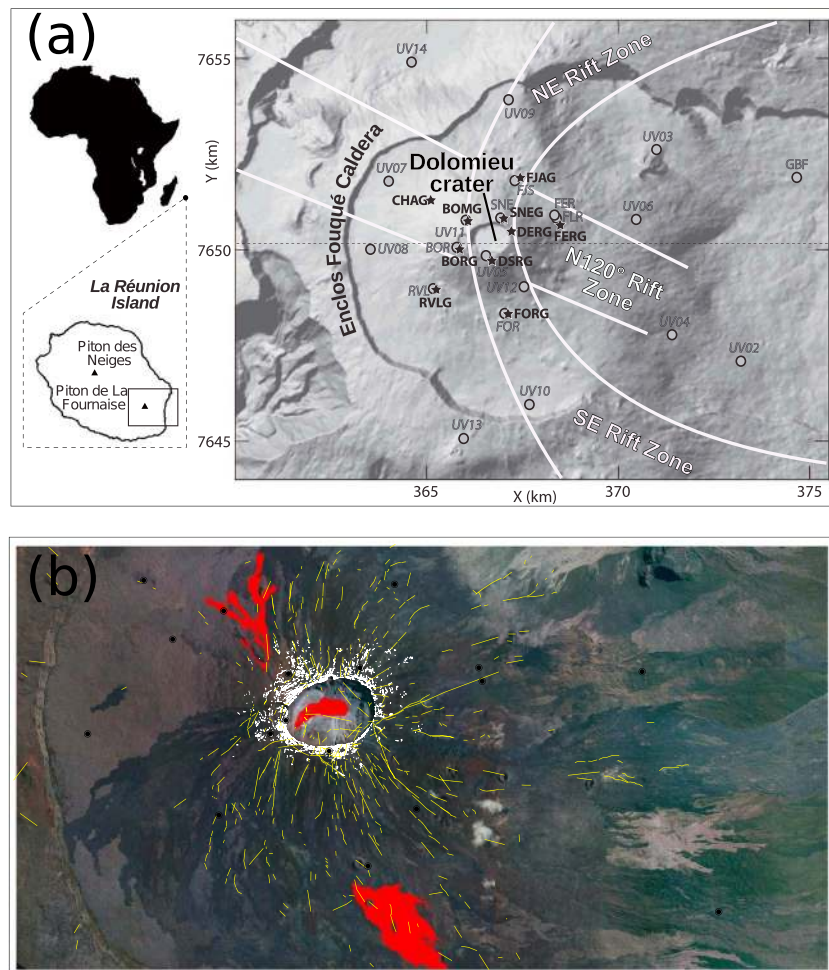
Figure 1. (a) Topographic map of the study region including locations of seismic stations (circles) and CGPS stations (stars) used in this study. (b) Map of fissures (yellow), fractures (white), and 2010 lavas (red; summit: January, south: October, north: December); black circles are the OVPF seismic stations, also shown in Figure 1a.

Piton de La Fournaise (OVPF) since 1980 [*Peltier et al.*, 2009b; *Roult et al.*, 2012] (Figure 1). It is considered to be caused by a hot spot [*Duncan et al.*, 1989], and its regional stress is small compared to the stress from the volcano itself [e.g., *Peltier et al.*, 2009a; *Sapin et al.*, 1996]. It lies in the Mascareignes Basin, which was formed by an extinct oceanic ridge [*Bernard and Munschy*, 2000]. The nearest measurements in the World Stress map database [*Heidbach et al.*, 2008] are from the mid-ocean ridge, where they tend to be perpendicular to the ridge segments, and from Madagascar, where two focal mechanisms yield nearly perpendicular directions of maximum horizontal stress, one strike slip and the other normal faulting [*Barth et al.*, 2007; *Shudofsky*, 1985]. Eruptive fissures and fractures on the volcano flanks tend to be oriented radially to the central cone, while fractures at the summit of the volcanic cone are oriented parallel to the summit caldera cliffs, that is, transverse to the ones on the flank (Figure 1b) [*Bachèlery*, 1981; *Michon et al.*, 2013]. A recent review of dike distribution in the walls of the summit caldera shows that summit dikes are preferentially oriented parallel to the N25–N30 and N120 rift zones [*Michon et al.*, 2013].

1.2. Previous Studies of Piton de la Fournaise

Volcanic eruptions on Piton de La Fournaise have occurred on average once per year over the last 35 years, with two periods of frequent activity from 1972 to 1992 and 1998 to 2010. A detailed analysis of records from 1985 to 2010 determined the timing and locations of past eruptions and seismic crises that may be caused by magmatic intrusions. The analysis delineated a series of precursors to the eruption in the form of accelerating tilt signals that may be related to stress changes [*Roult et al.*, 2012]. In addition, precursory patterns of
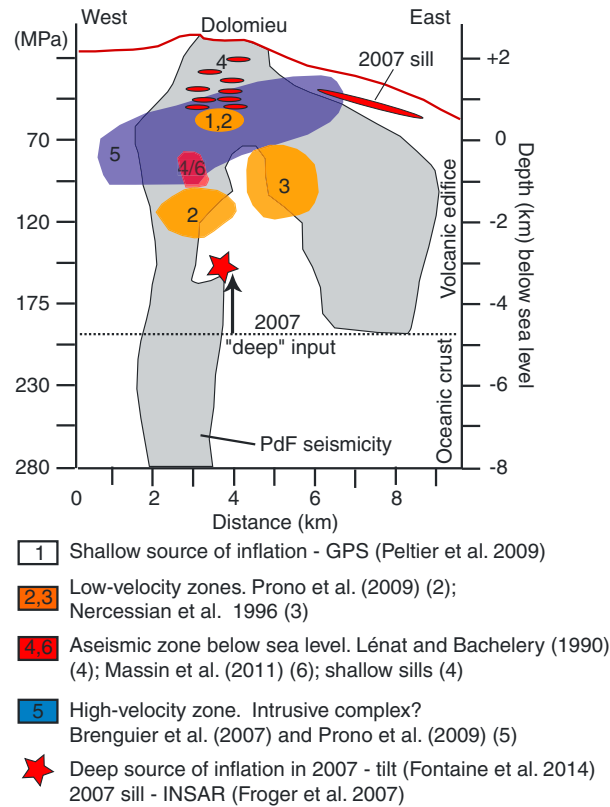
Figure 2. Interpretation of structure of Piton de la Fournaise volcano according to *DiMuro et al.* [2014]. Gray zones represent distribution of earthquake hypocenters. Star: source of inflation in 2007 from tilt [*Fontaine et al.*, 2014], which is considered to be a source of new magma that triggered the eruption. 1: source of inflation from GPS [*Peltier et al.*, 2009a]; 2, 3: low-velocity zones [*Nercessian et al.*, 1996; *Prôno et al.*, 2009]; 4: Network of shallow sills; 5: high-velocity zone suggested of intrusive complex [*Brenguier et al.*, 2007]; 6: aseismic zone below sea level [*Lenat and Bachelery*, 1990; *Massin et al.*, 2011]. Zones 4 and 6 are possible magmatic storage zones. The cross section starts from 0 at the edge of the Enclos Fouqué Caldera. GPS stations BORG and seismic station BOR are located at 3 km. DERG is at 4.3 km and FERG and FER are at 5.6 km.

seismicity, geodetic displacements, and seismic velocity changes were determined for 22 eruptions between 1999 and 2006. Different characteristic space and timescales were discovered for each of the observations [*Schmid et al.*, 2012]. Most eruptions occurred within the Enclos Fouqué caldera, with many in the Dolomieu crater on top of the summit cone. Between 2000 and 2007, eruptions followed a similar pattern; long-term precursors consisting of 1–5 months of summit inflation and strong seismic activity (up to 100 events per day) preceded cycles of successive eruptions. During eruptions, earthquake occurrence rates are high and are accompanied by a phase of increased eruptive activity. Eruption cycles usually start with summit and near-summit eruptions and end with a low-altitude eruption on the eastern flank of the volcano, along the NE and SE rift zones [*Got et al.*, 2013; *Peltier et al.*, 2009a]. However, on 2 April 2007, a much larger eruption on the southeast flank ejected about 10 times more material than any of the earlier ones, causing a summit crater collapse [e.g., *Massin et al.*, 2011; *Peltier et al.*, 2009b; *Staudacher et al.*, 2009]. This eruption was preceded by widespread flank movement occurring with injection of magma a few days prior to the eruption [*Clarke et al.*, 2013]. Eruption of shallow-seated magmas (above sea level) and part of the intrusive olivine-rich complex was triggered by a new input of deeper magma [*Di Muro et al.*,

2014; *Fontaine et al.*, 2014]. In general, the extrusion of shallow-seated magmas at PdF is triggered by magma emplacement at greater depths (Figure 2). *Sapin et al.* [1996] found earthquake focal mechanism reversals on the volcano that were associated with eruptive activity and postulated that the stress state changed with time. Focal mechanisms on the PdF volcano tend to be strike slip, despite being related temporally and spatially to magma transport [*Sapin et al.*, 1996]. A detailed analysis of focal mechanisms from multiplets associated with the 2007 sequence suggests that the strike-slip fault planes are oriented radially to the summit. Normal and reverse faulting also occurs, with nondouble couple mechanisms occurring just prior to the collapse of the crater [*Hirn et al.*, 1991; *Massin et al.*, 2011].

Cross-correlation of seismic noise records has determined that surface wave propagation speeds change with time, often decreasing just before eruptions, and may provide an additional precursory signal that is interpreted as an increase in crack density prior to the eruptions [*Brenguier et al.*, 2011, 2008; *Clarke et al.*, 2011; *Rivet et al.*, 2014]. The 2007 collapse was accompanied by a rapid decrease in wave speed followed by a slow increase, probably due to cracks first opening and then healing [*Clarke et al.*, 2013]. In 2010, a network of 15 broadband seismometers was installed to supplement the permanent network [*Brenguier*, 2012]. The most complete eruption sequence recorded by the network was the 14 October 2010 seismic crisis and eruption [*Schmid*, 2011] (Figures 1b and 3b). The seismicity included 800 events starting at 00:00 UT, but the crisis

(a) 2000-2013 Earthquake Locations colored by multiplet

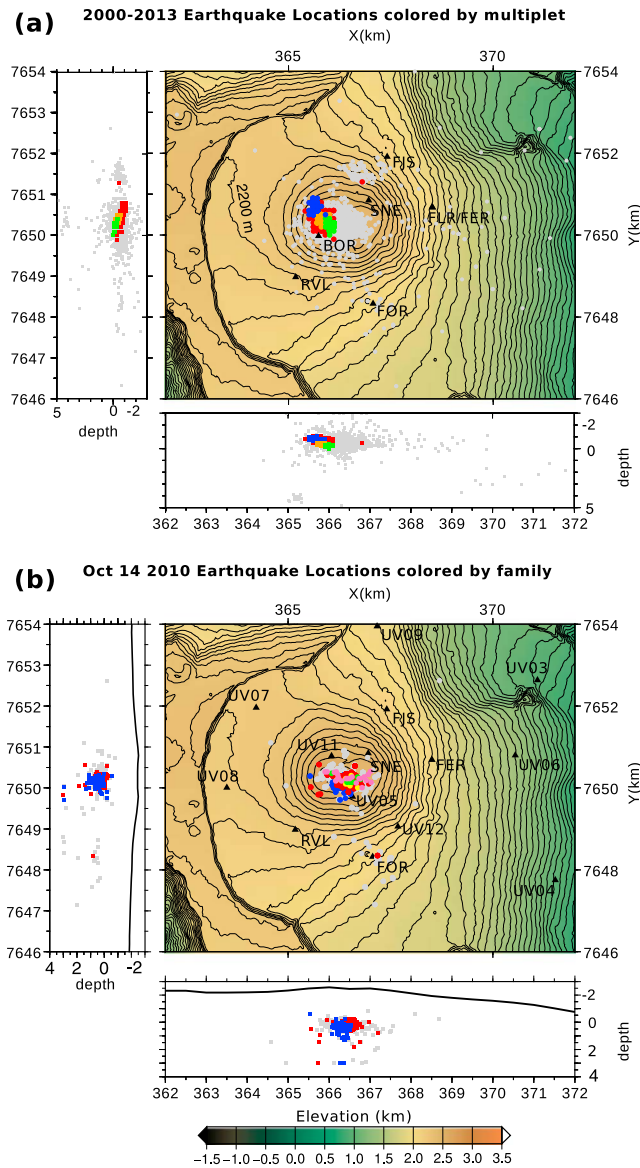**(b)** Oct 14 2010 Earthquake Locations colored by family

Figure 3. Map and cross sections of seismicity. Contour intervals are 50 m. The 2200 m contour is labeled. The x and y coordinates are distances in Réseau Géodésique de la Réunion 1992 (RGR92) format, with distances measured in kilometers [Reunion, 2008]. (a) All earthquakes in this study (i.e., from 2001 through 2012) that returned high-quality splitting measurements at some station. Labeled triangles show the permanent station locations to give an idea of the coverage through the bulk of the time period. Colors are the locations determined from the four multiplets with the highest number of events determined at BOR between 2000 and 2007. The multiplet locations shown are original locations before relocation, so the extent of the multiplets gives an indication of the error in the rest of the measurements. (b) Seismicity on 14 October 2010. Labeled triangles are the stations used in the locations. Red are in family 1, blue in family 2, and gray were in neither family. Yellow, green, and pink are the epicenters of earthquakes used in the focal mechanism analysis in Figure 9, colored by colors of the respective time periods. Errors in locations are in the order of 100 m.

itself is considered to have started at 09:45 and lasted 5 h and 35 min [Roult et al., 2012]. Gas composition for the October 2010 eruption suggested the possible involvement of external water-rich fluids at the beginning of the eruption [Allard et al., 2011].

2. Methodology

2.1. Seismic Data

We use two types of earthquake recordings to examine anisotropy: those from routine monitoring of the permanent network and some from special studies. We use earthquakes recorded on the six stations of the permanent network between October 2007 and December 2012 that were located on the volcano and had good S arrivals as determined using the routine processing system (Figures 1a and 3a). Stations that were too far from the study region or were located in lava tubes, which might disturb the measurements, were left out of the analysis.

For the permanent network monitoring, the P and S arrival times were picked by hand and used to locate the earthquakes, using a version of Hypo71 that was modified to incorporate topography to determine an initial source location before a three-dimensional tomographic study was carried out [Nercessian et al., 1996]. It is the same method and uses the same velocity model as used in the study that first suggested reversals of focal mechanisms at PdF [Sapin et al., 1996]. The velocity model (Table S1 in the supporting information) is a layered model extending above sea level, with a Vp/Vs ratio of 1.75 in each layer. Comparing catalogue locations to those from a special study using cross-correlation, the errors in the network locations are considered to be on the order of 250 m horizontally, 300 m vertically, and 0.09 s in time [Massin et al., 2011].

During times of regular seismicity, analysts pick and locate all events individually if possible. In the event of a seismic crisis, the largest events are picked alongside events that display significant difference in character to

those preceding them in order to ascertain hypocenter location changes over time. These locations are complementary to multiplet analysis. Figure 3a shows all the earthquake locations that gave good splitting measurements. We also consider three special datasets:

1. First is a set of 25 multiplets including 1764 events, determined at station BOR from January 2000 to July of 2006 [*Rivemale et al.*, 2010]. Multiplets are defined as sets of repeating earthquake with highly similar waveforms. The four multiplets with the highest numbers of good measurements (Multiplets 1–4) are shown as colored circles in Figures 3a.
2. Second are 527 multiplets determined between January and August of 2007, including a total of 1644 repeating earthquakes recognized on three permanent stations [*Massin et al.*, 2011].
3. Third is a set of 447 earthquakes located during the seismic crisis of 14 October 2010, which were recorded on the UnderVolc seismic network and located with the program NonLinLoc [*Lomax*, 2007; *Lomax et al.*, 2000; *Schmid*, 2011] (Figure 3b).

In each of the multiplet studies, precise arrival times were determined from the maximum correlation coefficients in cross-correlations between vertical component *P* waveforms of event pairs on common stations, with each study using slightly different methodologies and thresholds. The earthquakes within a multiplet have relative locations on the order of one source size from each other (~100 m) and are expected to have similar focal mechanisms. Earthquakes for the *Rivemale* [2010] study are gathered into multiplets using cross-spectral analysis and waveform coherency computations on the vertical component of the seismograms and Eardley's equivalence class algorithm [*Got et al.*, 2011, 1994]: an earthquake belongs to a multiplet if it has a coherency greater or equal to 90% with another earthquake of the multiplet. This procedure [*Got et al.*, 2011, 1994] was also used to compute the relative positions of the multiplet events. The multiplets from *Massin* [2011] were determined using a cross-correlation analysis to estimate *P* and *S* wave coherency on three permanent seismic stations and a partitioning algorithm to group repeating earthquakes into multiplets. Two pairs of events were merged into one multiplet if they involved a common earthquake and if they reached a cross-correlation coefficient threshold of 0.85 using a 17 s long signal windows starting on *P* wave arrivals, on one of the three stations. Multiplets were clustered by merging pairs from the most to least coherent, and their double-difference travel times were used as inputs in the relative location procedure of *Waldhauser and Ellsworth* [2000]. Six hundred thirty-three earthquakes were relocated using at least 12 double-difference travel times with a median RMS of 0.018 ± 0.012 s on cross-correlated waveforms. In the routine location results, repeating earthquake pairs have a median distance to their multiplet centroids of 0.32 ± 1.45 km. The relocation improves the median distance to 100 ± 220 m.

For 14 October 2010, earthquakes were divided into two families, F01 and F02, classified by detections on station UV11 only, as part of a broader study of the region [*Battaglia and Brenguier*, 2011]. Each waveform is included in a family if it crosses a correlation threshold that is fixed at 0.8. These two families make up the east and west halves of a structure that is located at sea level (Figure 3b). Only broadband stations were used in this study and so long-running station BOR was not included.

2.2. Shear Wave Splitting

Shear wave splitting is the seismic analogue of optical birefringence. It occurs when a shear wave, which has particle motion at an angle (ϕ_{in}) in a plane perpendicular to the propagation direction, enters an anisotropic medium. For rays emanating from an earthquake source, ϕ_{in} is set by the focal mechanism. The wave splits into two components, with polarization governed by the anisotropic properties of the medium as well as the propagation direction [e.g., *Babuska and Cara*, 1991]. During propagation, the two components become increasingly separated by a time delay (dt). The measured parameters are ϕ_{in}, dt, and the polarization of the fast direction, ϕ, but usually the focus is on the two parameters (ϕ and dt) that are most clearly caused by anisotropy.

We use the automatic shear wave splitting code MFAST [*Savage et al.*, 2010a] to calculate shear wave splitting. This code uses waveforms with *S* arrival times delineated to determine the optimum frequency for analysis. The optimum frequency determines start and end positions of windows in which to apply the eigenvalue covariance methodology [*Silver and Chan*, 1991]. Finally, cluster analysis is used to determine the best measurement from among the windows [*Teanby et al.*, 2004]. We use MFAST version 2.0, which

incorporates a corrected version of the code for determining degrees of freedom and 95% confidence intervals [*Walsh et al.*, 2013]. We search for *dt* measurements between 0.0 and 0.4 s but only use results that return delay times less than 0.2 s in order to avoid potential cycle-skipped waveforms. Measurement grading is carried out to determine the quality of the measurements; here we use measurement qualities of B or better (AB). For most of the studies, we add a further criterion that considers the maximum value of the contour plot of eigenvalues of the corrected covariance matrix on the grid of possible delay time and fast directions. The eigenvalues are normalized so that a value of 1 is the 95% confidence interval and higher values are multiples of that. The best measurements have large numbers of contour intervals, indicating that the 95% confidence is well separated from the larger, poorer, values. The "eigenvalue" criterion considers the largest eigenvalue, "emax." We use the selection criterion emax > 5 for static averages and correlations of parameters from the permanent stations and emax > 3 for moving averages and for correlations of parameters with fault plane solutions to allow more measurements.

In order to better compare measurements with each other using the same criteria, we also ran analyses with fixed filters. We used filters of 1–8 Hz and 4–10 Hz, since they were the ones most commonly chosen by the MFAST algorithm.

To calculate means, standard errors, and standard deviations for orientations ϕ and ϕ_{in}, we follow the method of *Gerst* [2003] who applies the directional statistics of *Mardia* [1972]. Normalized vectors of individual ϕ are multiplied by a factor of 2 and summed, and then the total length of the vector is divided by the number of measurements. The orientation of **R**, the resultant vector, is twice the mean ϕ, and its length $(0 < |\mathbf{R}_{mean}| < 1)$ is used to calculate the standard error and standard deviation. A length of 1 corresponds to all ϕ being the same, and a value of 0 represents a random distribution.

S to *P* wave conversions at the surface can interfere with shear wave splitting measurements if the wave's incidence angle at the surface (measured from vertical) is larger than the critical angle, which is about 35° for homogenous Poissonian solids. This angle extends to 45° because near-surface velocities are usually lower than velocities near the earthquake hypocenters, causing rays to bend to near vertical [*Booth and Crampin*, 1985]. For areas with particularly low surface velocities, it is even less of a problem because almost all rays arrive within 35° (e.g., at volcanoes [*Savage et al.*, 1989] and ocean bottom seismometers [*Volti et al.*, 2005]). Therefore, for most of this study, we do not restrict the incidence angle, although we test the assumption by separately considering results with straight-line incidence angles restricted to 45° and by examining the correlation between incidence angles and other parameters (see section 4.1.1). Station BOR, which has the most measurements, has most of its incidence angles less than 45° (1076 out of 1286; Tables 1 and S2), because it is on the central cone directly above most of the seismicity (Figure 3).

2.3. Comparison Data sets

To calculate Vp/Vs ratios, we use the method of *Nur* [1972], with Vp/V$_S$ = ts/tp, where ts = $T_S - T_0$ and tp = $T_P - T_0$, where T_S and T_P are the arrival times of the *S* and *P* waves, respectively, and T_0 is the origin time of the earthquake determined during the location procedures described above. The errors in these ratios depend upon the errors in the values used to determine them and will be dominated by the errors in origin time. Using errors of ±0.09 s in origin time, formal error analysis suggests errors in the ratios could be up to 25% for individual measurements, which will decrease for the average depending on the numbers of measurements. The standard deviation of the means ranges from 0.03 to 0.19, that is, up to 10% (Table 1).

We used the HASH program [*Hardebeck and Shearer*, 2002] to calculate focal mechanisms for the 41 largest magnitude events in the sequence. Daily solutions of GPS data were processed using the GAMIT/GLOBK software package. This software considers the precise International GNSS Service (IGS) ephemeris, a stable support network of IGS stations, a tested parameterization of the troposphere, and models of ocean loading and Earth and lunar tides. These considerations increase the precision of the solution (about 2 and 5 mm on the horizontal and vertical components, respectively). We also computed kinematic solutions for each epoch of measurements (every 30 s) during the eruptive days to highlight rapid variations. See *Staudacher and Peltier* [2015] for more detail.

For the 4–10 Hz frequency set of splitting measurements, we compare each variable reported by MFAST to other variables. We used the AB quality measurements that had an emax >5. To compare splitting

Table 1. Measurements from 4 to 10 Hz Band[a]

staname	nmeas	ϕ	stderr(ϕ)	stdev(ϕ)	R_{mean}	dt	stderrdt	ϕ_{in}	R_{mean} (ϕ_{in})	stderr (ϕ_{in})	stalat	stalon	Azimuth from Central Crater	vpvs	vpvsstdev
BOR	1286	46.4	1.5	41.2	0.35	0.080	0.001	−27.6	0.21	2.6	7649.982	365.733	247	1.82	0.19
FER	389	48.4	1.6	30.6	0.57	0.088	0.002	81.2	0.24	4.2	7651.309	367.867	53	1.66	0.16
FJS	566	28.3	1.0	24.4	0.70	0.088	0.001	−64.9	0.20	4.2	7651.918	367.405	27	1.67	0.08
FLR	174	64.4	2.3	29.2	0.59	0.084	0.003	−63.9	0.32	4.7	7650.682	368.513	80	1.65	0.09
FOR	487	4.7	1.1	24.8	0.69	0.079	0.001	70.1	0.54	1.5	7648.325	367.061	168	1.62	0.08
GBF	31	−84.6	6.2	31.8	0.54	0.061	0.008	71.1	0.26	14.0	7651.755	374.974	81	1.68	0.03
PBR	13	−1.8	18.0	44.2	0.30	0.100	0.014	34.6	0.12	48.0	7653.679	360.339	−62	1.86	0.28
RVL	528	37.3	0.9	20.0	0.78	0.080	0.001	−86.8	0.34	2.5	7648.977	365.17	226	1.66	0.10
SNE	425	42.6	5.0	51.8	0.19	0.073	0.002	58.9	0.10	9.6	7650.849	366.958	35	1.82	0.13
UV01	5	8.5	10.3	23.1	0.72	0.123	0.007	−41.9	0.93	4.9	7650.29	360.212	269	1.72	0.05
UV02	11	−68.7	9.1	29.0	0.60	0.070	0.012	22.8	0.35	17.1	7647.052	373.364	116	1.71	0.04
UV03	43	73.6	5.0	30.9	0.56	0.095	0.007	−3.2	0.37	8.0	7652.626	371.088	63	1.72	0.08
UV04	29	−80.7	3.4	18.7	0.81	0.093	0.014	−69.3	0.67	4.8	7647.753	371.52	118	1.70	0.05
UV05	22	49.3	22.6	52.3	0.19	0.069	0.010	6.6	0.36	11.7	7649.794	366.571	184	2.06	0.25
UV06	36	53.2	3.4	20.5	0.77	0.089	0.005	30.3	0.20	16.8	7650.803	370.546	84	1.69	0.08
UV07	45	−19.9	8.6	41.9	0.34	0.063	0.005	82.0	0.33	8.8	7651.962	364.217	−56	1.70	0.06
UV08	92	81.2	5.5	40.4	0.37	0.079	0.005	3.1	0.11	19.9	7650.012	363.499	264	1.71	0.06
UV09	19	0.0	14.9	44.2	0.30	0.115	0.010	56.3	0.39	11.3	7653.952	367.173	9	1.71	0.07
UV10	65	−28.6	3.2	25.3	0.68	0.071	0.004	53.2	0.09	26.8	7645.916	367.732	166	1.74	0.08
UV11	61	−29.1	7.2	41.5	0.35	0.105	0.008	30.8	0.52	4.6	7650.776	366.057	−53	1.74	0.14
UV12	109	−37.0	2.3	24.1	0.70	0.095	0.003	−79.6	0.33	5.7	7649.059	367.68	141	1.65	0.11
UV13	34	40.7	14.1	48.3	0.24	0.083	0.007	−70.3	0.04	84.5	7645.026	365.97	187	1.77	0.06
UV14	14	1.4	5.1	19.4	0.79	0.069	0.008	73.0	0.07	74.9	7654.956	364.589	−24	1.69	0.05
UV15	27	−1.8	6.1	30.3	0.57	0.107	0.009	65.6	0.27	14.1	7650.179	366.023	253	1.81	0.11
mean					0.530	0.086								1.74	
std					0.200	0.016								0.09	

[a]Headings are defined as follows: nmeas, number of measurements; stderr, standard error; stdev, standard deviation. The azimuth from the central crater is calculated from the station latitude and longitude and the deepest point of the crater, at X: 366.613, Y: 7650.360 (longitude 55°, 42′, 41.6″, latitude 21°, 14′, 38″). In the course of the study, we discovered that seismometer station FJS was misoriented. The orientation that was reported as north was in fact oriented −53° (53° west of north). We have corrected the orientation in the tables and figures presented here. The seismometer remains in that position.

Table 2. Measurements from 1 to 8 Hz Band

Staname	nmeas	ϕ	stderr(ϕ)	stdev(ϕ)	R_{mean}	dt for 1–8 Hz	stderrdt	ϕ_{in}	R_{mean} (ϕ_{in})	stderr(ϕ_{in})
BOR	609	40.9	2.2	40.7	0.36	0.073	0.002	−25.3	0.23	3.5
FER	247	49.8	1.7	26.1	0.66	0.078	0.003	88.2	0.35	3.6
FJS	292	19.4	1.3	22.4	0.74	0.098	0.002	−25.0	0.23	5.0
FLR	27	70.7	4.5	23.3	0.72	0.074	0.010	−84.3	0.69	4.8
FOR	286	−10.3	1.5	25.1	0.68	0.075	0.002	33.1	0.32	3.7
GBF	14	−83.4	16.8	43.6	0.31	0.035	0.010	69.2	0.37	14.0
RVL	344	39.0	0.9	16.0	0.85	0.079	0.001	−87.7	0.55	1.8
SNE	405	−5.6	3.0	43.1	0.32	0.071	0.002	31.6	0.39	2.5
UV01	2	6.5	14.2	20.3	0.78	0.139	0.021	−65.3	0.52	25.5
UV02	2	−71.5	4.6	6.5	0.97	0.130	0.049	−15.1	0.98	3.6
UV03	24	61.8	3.7	18.4	0.81	0.109	0.008	−12.6	0.30	13.3
UV04	28	−86.3	3.8	20.5	0.77	0.121	0.013	−81.7	0.49	7.2
UV05	4	−9.5	1.8	3.5	0.99	0.113	0.041	−8.3	0.73	11.3
UV06	16	51.8	4.9	20.1	0.78	0.072	0.006	87.8	0.69	6.1
UV07	24	−10.7	9.5	38.0	0.41	0.052	0.008	−81.4	0.47	8.3
UV08	58	75.6	2.6	20.3	0.78	0.094	0.005	21.2	0.33	7.7
UV09	10	23.9	2.9	9.1	0.95	0.104	0.013	66.7	0.92	3.7
UV10	36	−51.4	6.7	35.1	0.47	0.059	0.004	56.5	0.23	14.8
UV11	10	−73.8	35.5	53.1	0.18	0.108	0.023	62.0	0.21	29.8
UV12	92	−39.7	1.8	17.7	0.83	0.096	0.003	−70.5	0.37	5.4
UV13	18	57.6	14.0	42.5	0.33	0.102	0.011	−57.3	0.10	49.9
UV14	10	−16.4	7.0	22.3	0.74	0.049	0.008	−34.1	0.66	8.4
UV15	18	−48.9	14.9	43.7	0.31	0.156	0.008	−79.5	0.65	6.3
Mean					0.642	0.091				
Std					0.24	0.0294				

measurements to GPS and isotropic velocity change *dV/V*, we start by computing daily averages of each measurement type separately. Then on days with splitting measurements, we find the nearest day's GPS and *dV/V* data to compare. To calculate the correlation coefficients, we use the MATLAB statistical toolbox for the nonangular variables. For angular variables, we use a directional statistics package, also written in MATLAB [*Berens*, 2009]. We report zero-lag correlation coefficients (*c*) normalized between 0 and 1, with 0 being uncorrelated and 1 being a perfect correlation. Correlation *p* values (*p*) represent the likelihood that a distribution will occur by chance, and a *p* value less than 0.05 is statistically significant.

3. Results

In most cases, we find that the stations near the summit of the cone (UV11, BOR, UV05, and SNE; Figures 1 and 3) behave differently from those near the base of the cone (FOR, RVL, FJS, FER, FLR, and UV12), near the edge of the caldera (UV07, UV08, UV09, and UV10), and the distal stations (UV02, UV03, UV04, UV06, UV13, UV14, and GBF). We will refer to these station groups as "summit," "base," "caldera edge," and "distal", respectively, in the following discussions. We consider the results in three ways: (1) as overall average results with spatial variation, in which we observe a pattern of radially symmetric fast directions and Vp/Vs ratios that are higher at summit stations than at base stations; (2) as a long-term function of time from 2001 through 2011, where we note systematic changes in delay time and fast direction that tend to correlate with geodetic measurements, isotropic velocities, and the occurrence of eruptions; (3) as a function of time for the eruption on 14 October 2010, where we find variations on the order of minutes to hours that also correlate with GPS and focal mechanism changes.

3.1. Average Results and Spatial Variation for All Measurements

Most of the earthquakes occur in a fairly small and shallow region under the summit (Figure 3). Tables 1 and 2 show the shear wave splitting results, and Figure 4 shows circular histograms (rose diagrams) displaying the spatial variation of ϕ for the highest-quality (emax > 5) measurements for both frequency ranges examined at all stations that yielded 10 or more measurements, including all time periods. The 4–10 Hz frequency range yielded more measurements than 1–8 Hz at all stations. Both sets of data have some stations with several
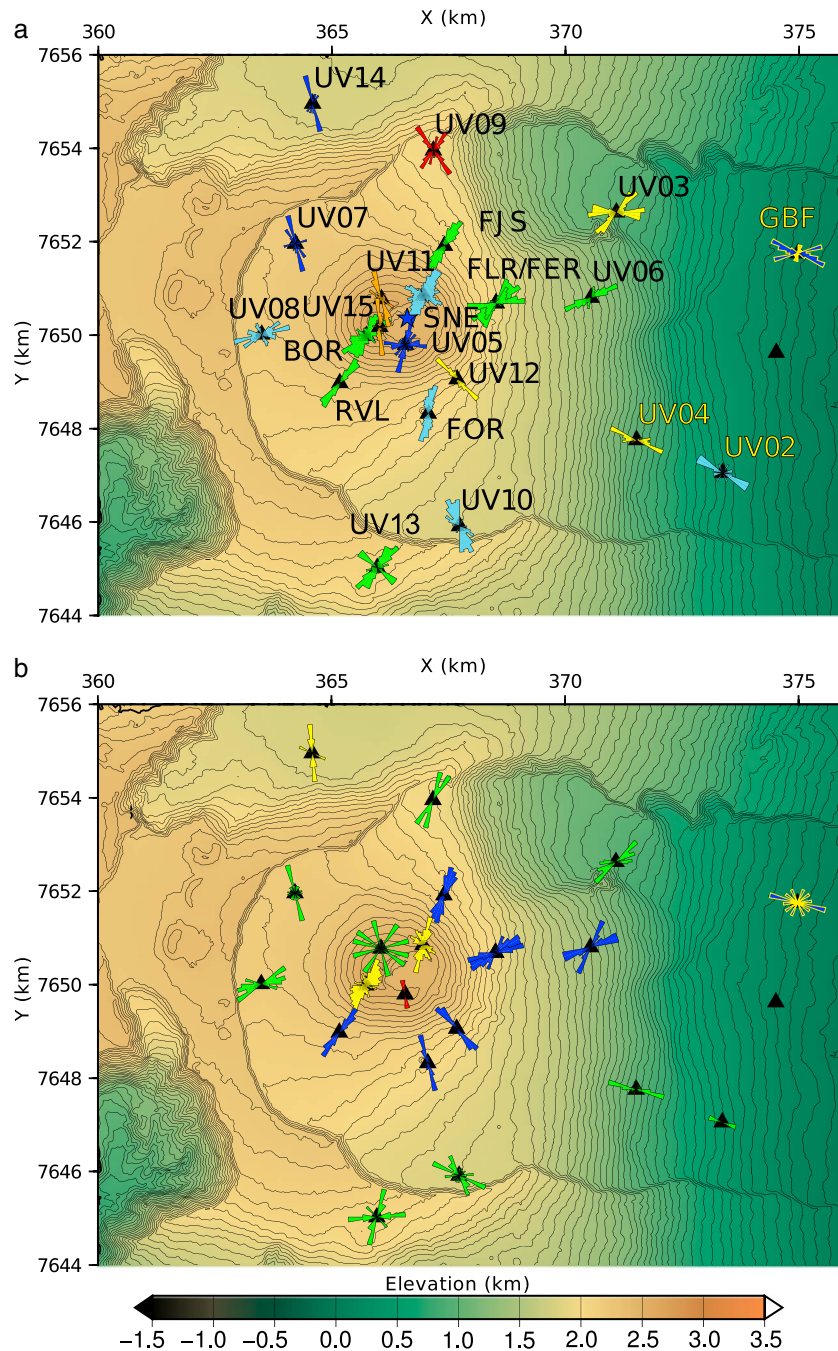
Figure 4. See also Tables 1 and 2. Polarization of the first arriving *S* wave for all high-quality measurements, including from permanent and temporary stations, during and outside of crises. The rose diagrams have the same length, and the numbers of events in each diagram are listed in Table 1. Only quality A and B measurements with emax > 5 are reported. Only stations with more than 10 such measurements are included. Most of the stations are within the Enclos Fouqué caldera (delineated by the extremely close error contours; see Figure 1 for place names). (a) 4–10 Hz. Roses are colored by the average delay time for the measurements: 0.06–0.07: navy blue, 0.07–0.08: light blue, 0.08–0.09: green, 0.09–0.10: yellow, 0.10–0.11: orange, and 0.11–0.12: red. The blue star is the location of the bottom of the Dolomieu crater, from which the azimuths are calculated. (b) Same as in Figure 4a except for 1–8 Hz and colors are for average station Vp/Vs ratios according to this scale: 1.6–1.7: blue 1.7–1.8: green, 1.8–1.9: yellow, 1.9–2.0: orange, and 2.0–2.1: red.

populations of measurements, but the higher-frequency set has stronger double peaks. This is reflected with slightly higher average R_{mean} for 1–8 Hz (0.6 ± 0.2) compared to 4–10 Hz (0.5 ± 0.2).

The circular histograms (rose diagrams) of the fast directions tend to be perpendicular to the contour lines, that is, radial to the central cone (Figure 4). To quantitatively assess this observation, we compare their azimuths from the center of the deflation that occurred after the 2007 collapse, which was nearly identical to the lowest elevation in the Dolomieu crater [*Staudacher et al.*, 2009]. Comparing the azimuths using circular statistics, if we only consider stations that have $R_{mean} > 0.5$ for 4–10 Hz, the average difference between the fast direction and the azimuth to the crater center is 19 ± 17° (±1 standard deviation). For 1–8 Hz, it is 13 ± 11. Stations at intermediate distances from the summit all have ϕ close to radial to the central crater. Even when there are two or more populations, one tends to be radial to the crater or parallel to the crater walls for stations on the summit, where cracks develop parallel to the rim (Figure 1b).

Base stations tend to have the lowest Vp/Vs ratios (<1.7; Table 1 and blue in Figure 4b). Stations at the outer edge of or outside the caldera tend to have Vp/Vs ratios around 1.7 (green). Stations on the summit tend to have high Vp/Vs ratios greater than 1.8 (yellow and red), with the exception of station UV11, which has 1.74. Some of the stations on the summit and NW rift zone have slightly higher delay times (Figure 4a, orange, red, and yellow at UV11, UV15, and UV09, respectively). Otherwise, the delay times do not have a strong a correlation with position. There is a slight negative correlation of delay times with frequency ($c = -0.12$; Table S3), reflecting a trend in all types of shear wave splitting data for delay times to be larger for longer-period waves [e.g., *Karalliyadda and Savage*, 2013; *Marson-Pidgeon and Savage*, 1997]. However, the use of a common filter has minimized the range of frequencies that are available to study, and dt for 1–8 Hz (0.09 ± 0.03 s) is not significantly different from dt for 4–10 Hz (0.09 ± 0.02 s) (Tables 1 and 2).

Vp/Vs has a weak negative correlation with epicentral distance ($c = -0.22$) (Table S3a). This may be because the Vp/Vs ratio is larger in the center of the cone, and most of the earthquakes are below the cone (Figure 3). Vp/Vs is also somewhat correlated with errors in measurements and negatively with SNR, which may mean that poorer measurements yield S arrivals that are too late. A variation of Vp/Vs with back azimuth ($c = 0.19$; Table S3b) is because of the spatial variation of Vp/Vs observed in Figure 4. The lack of correlation between dt and Vp/Vs reflects that some stations have positive correlations and others negative correlations between these parameters (see section 3.2)

Considering correlations between values for all the stations together (over 2900 measurements, dominated by station BOR because of its long running time), many variables have very low p values (i.e., they are significant) but have low correlation coefficients. If we consider only p values less than 0.05 (better than 95% confidence) and correlation coefficients $c > 0.2$, the latitude, longitude, distance, and depth are well correlated with each other, as is visible in Figure 3 and Table S3a. Also, many of the errors (standard deviations, σ) are correlated positively to each other and negatively to measures of quality of signal-to-noise ratio (SNR) and emax, for example, $\sigma(dt)$ with $\sigma(\phi_{in})$ and $\sigma(\phi)$ with $\sigma(\phi_{in})$ and $\sigma(dt)$. $\sigma(\phi)$ is also correlated negatively with delay time ($c = -0.44$), which is due to the fact that small delay times correspond to very little splitting and so the fast direction is not well determined. High correlations are also found for values that are physically related, such as epicentral distance and angle of incidence ($c = 0.46$), since most of the earthquakes are close to each other at similar (shallow) depths. SNR is weakly correlated to day of year ($c = 0.11$) probably due to seasonality in wind patterns.

The main measured parameters of fast direction, incoming polarization, delay time, and Vp/Vs are weakly correlated with each other (Table S3), due in part to the fact that changes in each of these parameters occur at the same times (see results below, section 3.2). Fast direction is weakly correlated with ϕ_{in} ($c = 0.194$), dt (0.08), SNR (0.08), and Vp/Vs (0.18). The correlation with ϕ_{in} is due to the requirement that all nonnull measurements must satisfy $70° > \phi - \phi_{in} > 20°$, which relates the two parameters. Incoming polarization ϕ_{in} is also weakly correlated with angle of incidence ($c = 0.175$) and dt (0.13). When error bars become large, falsely large delay times may be measured [e.g., *Savage*, 1999]. This explains weak correlations between dt and $\sigma(\phi_{in})$ ($c = 0.12$), SNR ($c = -0.08$), and emax ($c = -0.15$). The weak increase in dt with ϕ_{in} ($c = 0.13$) could reflect an artifact in the measurement, such as cycle skipping (see section 4.4).
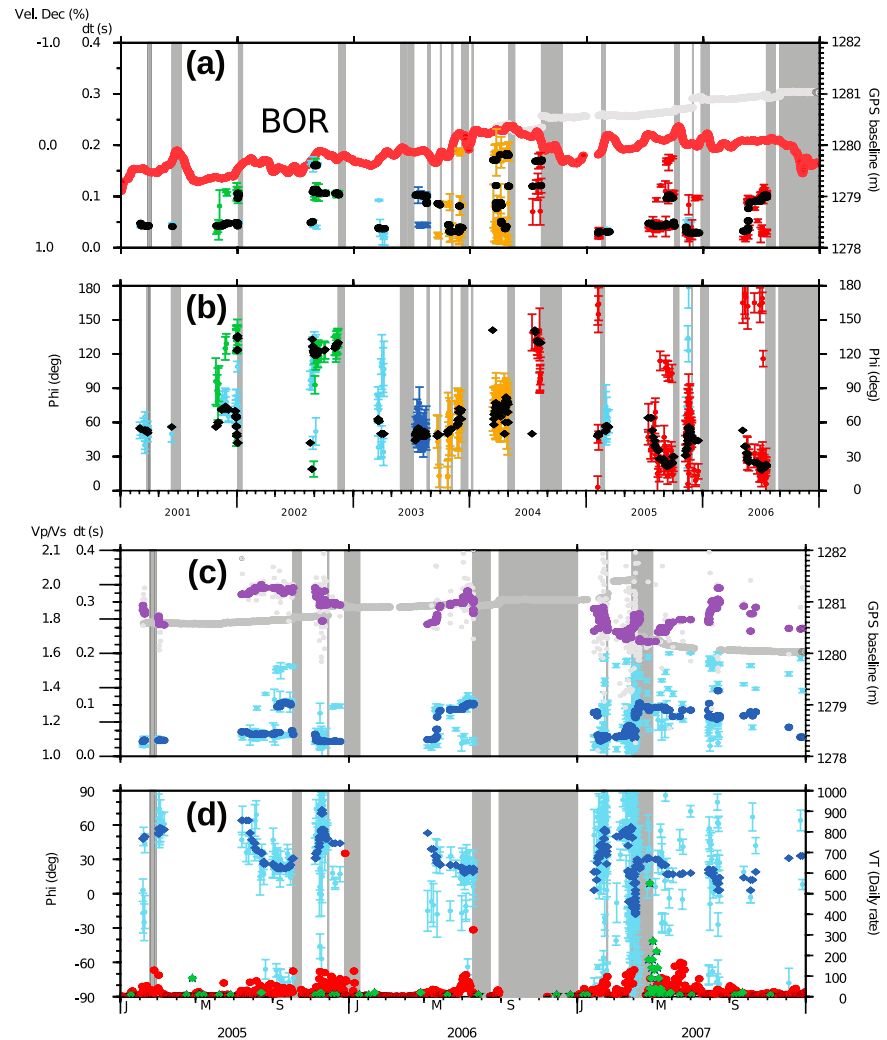
Figure 5. (a–d) Shear wave splitting measurements with time at station BOR. Vertical bars are eruption sequences (gray) or intrusions (red) [*Roult et al.*, 2012] with widths denoting the duration of the sequence. GPS baseline (light gray) between summit stations DSRG and SNEG, which span the caldera (Figure 1), is shown on *dt* plots in Figures 5a and 5c after 2004. Figures 5a and 5b show data from 2000 to 2007. Colors represent individual multiplets, corresponding to colors in Figure 3a, with gray values representing other clusters. Black circles and diamonds are 20-point moving medians. Figure 5a shows *dt* measurements. Average velocity decrease from noise cross-correlation [*Rivet et al.*, 2014] is shown by red circles. Figure 5b shows ϕ measurements. Figures 5c and 5d show data from 2005 to 2007. Sky blue circles and diamonds are individual measurements, and dark blue circles and diamonds are 20-point moving medians. Figure 5c shows *dt* and Vp/Vs ratio (light gray circles for individual points and purple circles for 20-point moving average). Figure 5d shows ϕ and rate of volcano tectonic earthquakes (red circles) and daily numbers of long-period earthquakes multiplied by 10 (green stars).

3.2. Results as a Function of Time

Changes in shear wave splitting in general correlate with previously noted changes in GPS and isotropic velocity, and with eruptions, and such correlation is observed through both the long-term studies and the special study of the 14 October 2010 swarm.

3.2.1. Long-term Variation

Summit station BOR operated longer than all other stations and represents the majority of the measurements. Figure S1 shows moving means of splitting parameters and Vp/Vs ratios for all the 1286 measurements for BOR, including the multiplets from 2000–2006 [*Rivemale et al.*, 2010] and 2007 [*Massin et al.*, 2011] as well from the standard network analysis (Table 1). Figure 5 shows moving medians for 2000–2007 along with the summit GPS
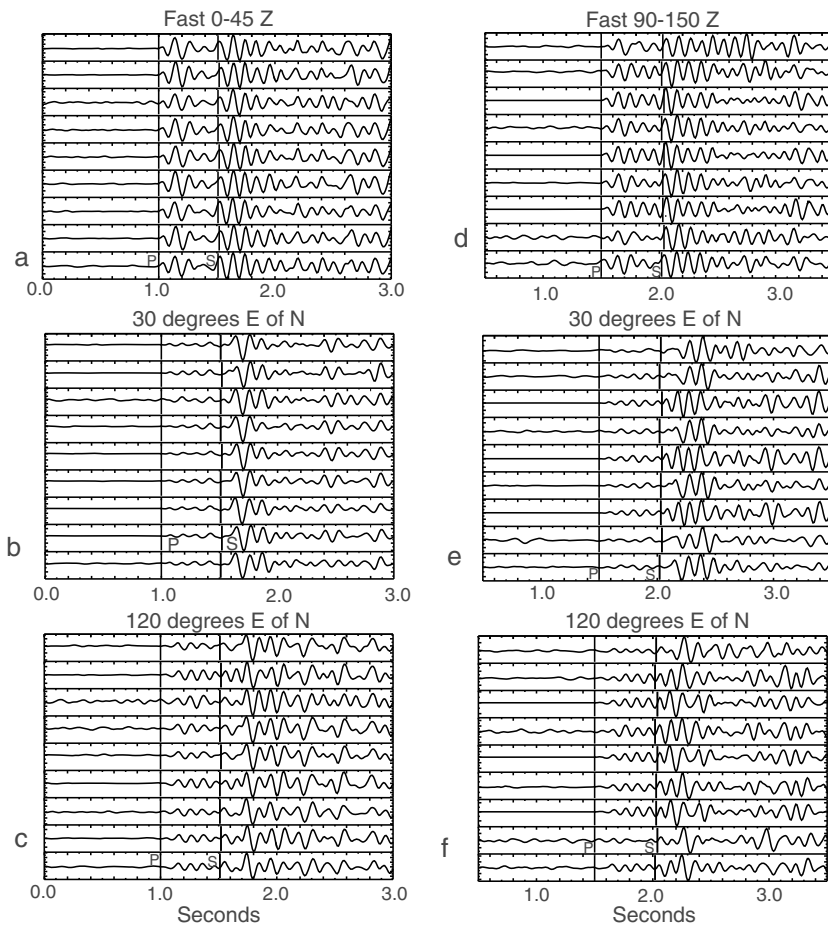
Figure 6. Comparison of waveforms from Multiplet 001 at BOR [*Rivemale et al.*, 2010] for the vertical component (*Z*) and the horizontal components oriented at 30° and 120°. Waveforms that (a–c) returned ϕ between 0 and 45 and (d–f) had ϕ of 90–150. The vertical waveforms are all similar, but the horizontal waveforms show clear differences.

baseline SNEG-DSRG and the isotropic velocity decrease as measured by noise cross-correlations [*Rivet et al.*, 2014]. The multiplets determined in 2000–2006 (Figures 5a and 5b) [*Rivemale et al.*, 2010] all stopped in 2007, presumably because the paths or sources were changed dramatically in the 2007 crater collapse and lateral flank sliding.

There are three main populations of *dt* measurements at around 0.05, 0.1, and 0.15 s, with a tendency for the numbers in the high delay time group to increase before eruptions between 2005 and 2007 and a slight increase in the average values of *dt* along with decreasing isotropic velocity from 2000 to 2004 (Figures 5a, 5c, and S1). Baseline lengths mainly increased before 2007, attesting to a region-wide summit inflation, with sharp increases accompanying many eruptions (Figure 5c). Correlations between baseline lengths and both delay times ($c = -0.35$) and velocity change ($c = 0.57$) are strong ($p < 0.00001$) (Table S3c). Correlations between *dt* and velocity changes ($c = -0.29$) and Vp/Vs and velocity changes ($c = 0.09$) are significant but not as large. The changes in populations of *dt* are accompanied by changes in ϕ, with ϕ measurement populations at about 60° and 120° before 2004 and between 60° and $-20°$ (160°) after 2004 (Figures 5b and 5d). Correlations between fast direction and *dt* ($c = 0.42$) and ϕ_{in} and *dt* ($c = 0.53$) are fairly strong ($p < 1e-10$) from 2000 to 2006 (Table S3c). Vp/Vs ratios have a general trend of increasing from 2000 through 2006: before 2007, Vp/Vs correlates with year as $c = 0.39$ with $p = 3.8e-20$. Over the same period, there is a positive correlation between Vp/Vs and *dt* ($c = 0.26$, $p = 5.7e-4$) (Figures 5c and S1 and Table S3).

The multiplet with the most measurements that was present over the longest time period is Multiplet 001 (red in Figures 3a, 5a, and 5b), which yielded 328 A and B quality measurements, of which 321 have
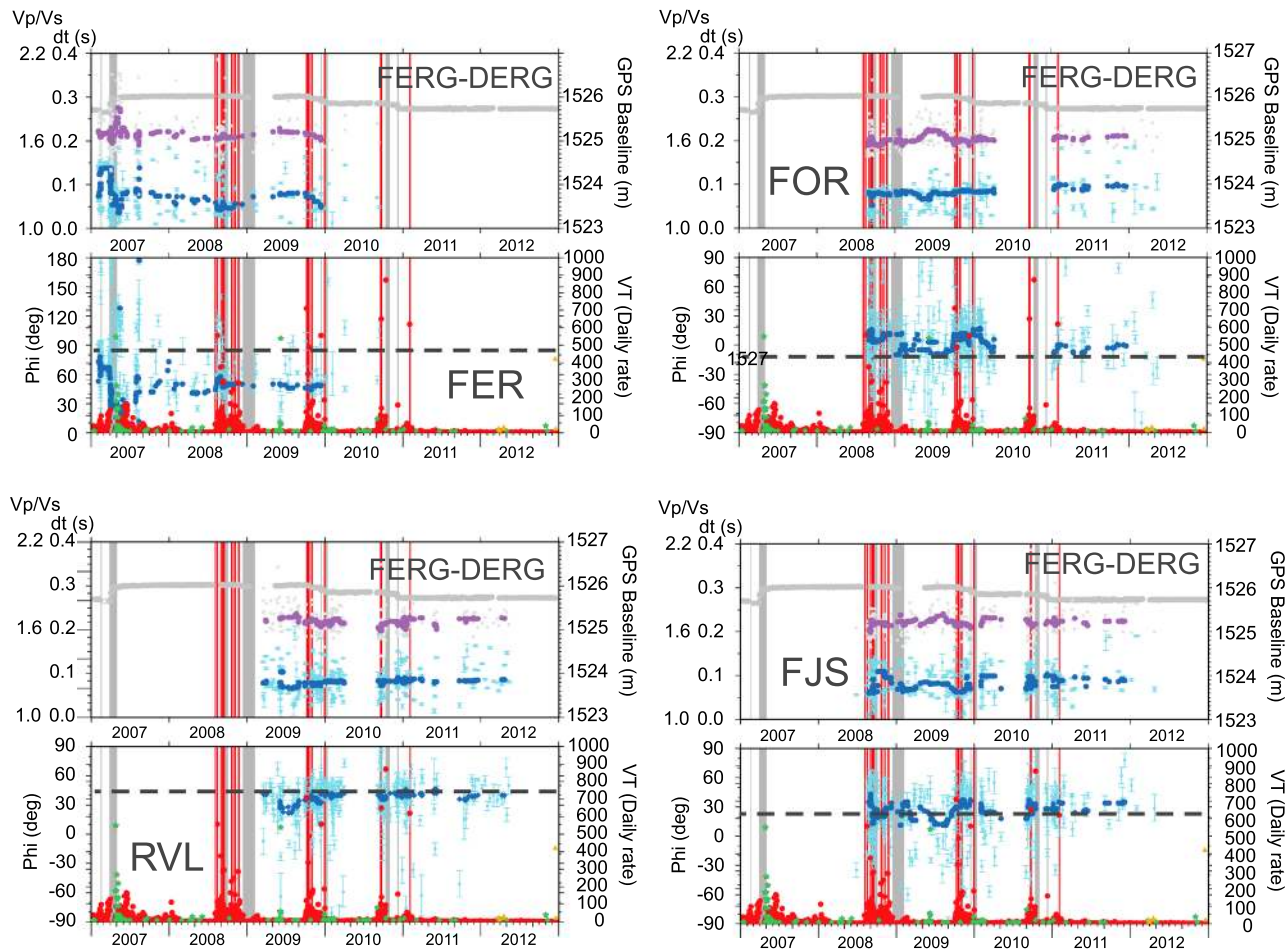
SUMMIT
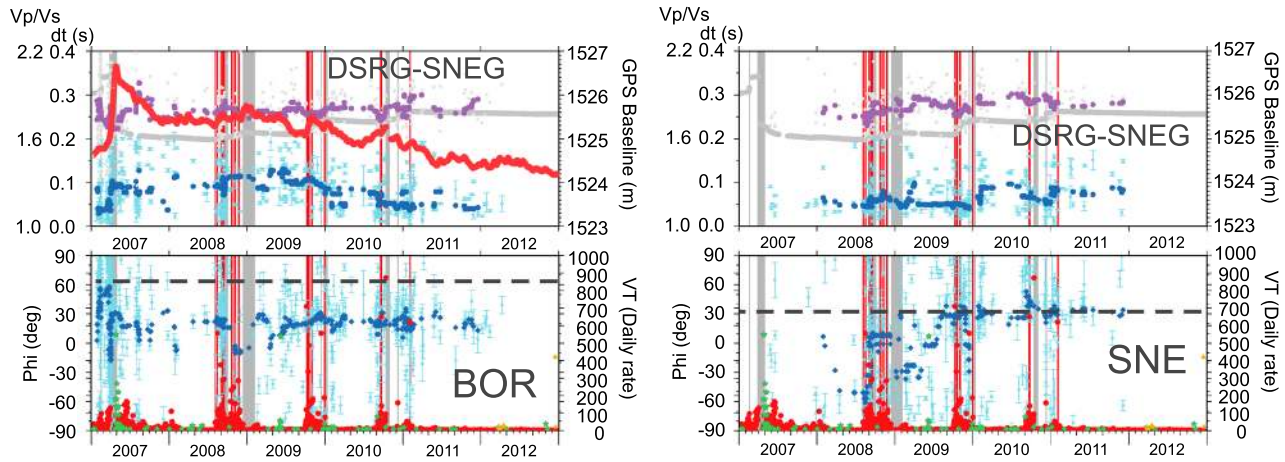
BASE

Figure 7. Shear wave splitting measurements with time and their moving medians at permanent stations operating between 2007 and 2012. Vertical bars are eruption sequences (gray) or intrusions (red) [*Roult et al.*, 2012], with widths denoting the duration of the sequence. Sky blue are individual measurements of ϕ or dt; dark blue are 20-point moving medians. Vp/Vs ratio (light gray circles for individual points and purple circles for 20-point moving average) is shown on the dt plot. Rate of volcano tectonic earthquakes (red circles) and daily numbers of long-period earthquakes multiplied by 10 (green circles) are shown on the ϕ plot. GPS baseline (gray circles) between summit stations DSRG and SNEG, which spans the caldera (Figure 1), is shown for summit stations BOR and SNE, while the baseline between FERG and DERG is shown on the stations at the base of the cone. On station BOR, the isotropic velocity change [*Rivet et al.*, 2014] is shown with red circles on the dt plot. As in Figure 5, the bottom of the plot represents a change in dV/V of +1.0% and the top of the plot represents −1%.
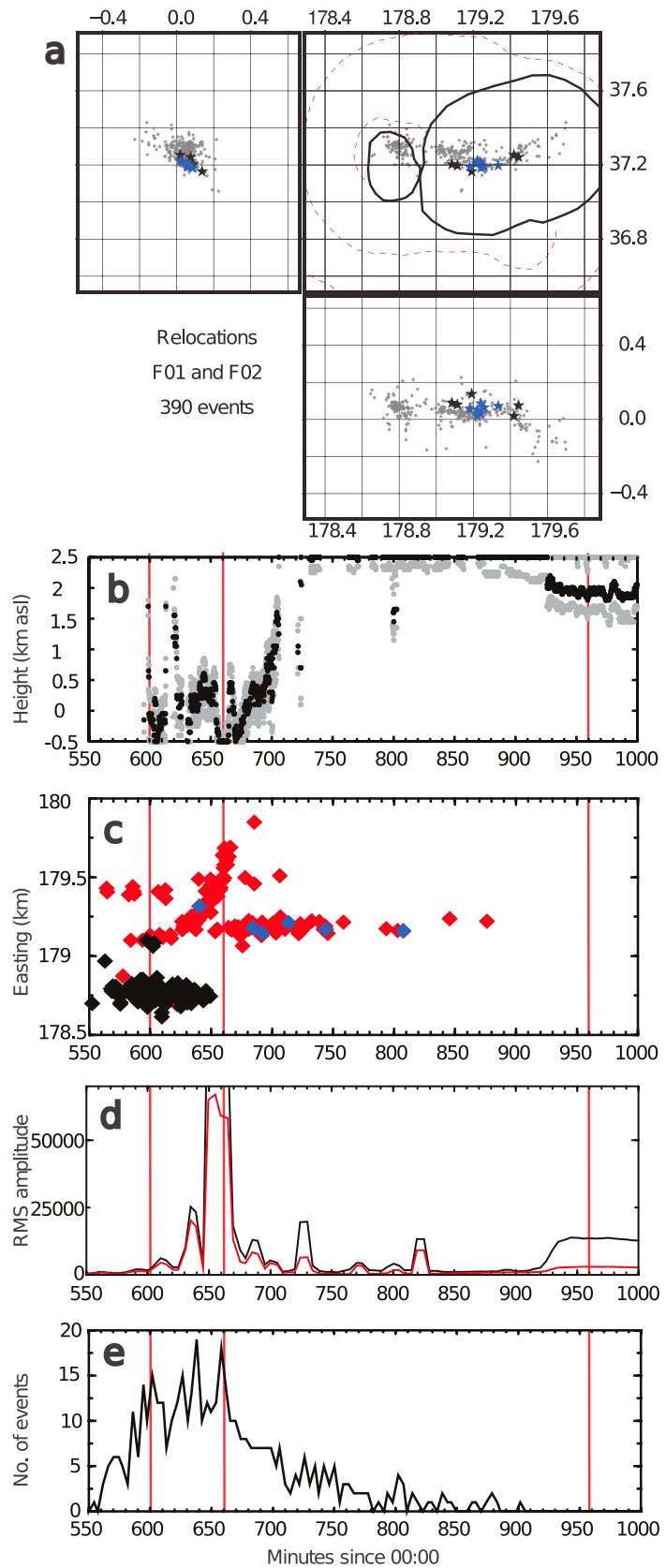
Figure 8

emax > 3 and 220 have emax > 5. Events in this multiplet had an average depth of 0.6 km above sea level with no systematic variation over time. The measurements on the multiplets include distinct populations of dt and ϕ (Figure 5). These populations are represented by waveforms that vary accordingly, despite having been identified as members of the same multiplet. For example, we consider Multiplet 001 for the vertical component and the horizontal components oriented at 30° and 120° (Figure 6). Waveforms that return fast directions between 0° and 45° have a different character from those with fast directions from 90° to 150°. The vertical waveforms are similar in both groups, but the horizontal waveforms show clear differences.

The behavior of many variables changed after the April 2007 Dolomieu crater collapse. At the time of the collapse, the summit GPS baseline decreased, isotropic velocity decreased, and at summit station BOR, dt values increased and ϕ rotated from 60° to 30° (Figures 5 and 7). In contrast, GPS baselines between summit and base stations increased, and dt on base station FER decreased, accompanied by a rotation from 60° to 30° in ϕ. Vp/Vs at BOR and FER fluctuated more during the time of the collapse than at other times. There is no strong correlation between rainfall and delay times (not shown), even though changes in the water table might change the proportion of liquid-filled cracks near the surface.

After these abrupt changes, some recovery toward previous values is apparent in isotropic velocity and dt at station BOR (Figure 7). Here dt increased slightly again and then remained constant until about mid-2009 and since then has been slowly decreasing; correlation between dt and year has $c = -0.42$ with $p = 1.7e{-}12$ from 2009 to 2012 (Figures S1 and 7). As expected, there is larger scatter after 2007, when earthquakes that were not multiplets were included. At BOR, there is a general inverse trend between baseline length between nearby summit GPS stations and delay times, with delay times increasing as baseline decreases and vice versa, yielding a correlation coefficient of $c = -0.51$ and p value less than 0.0001 (cf., early 2007, 2009, and 2010) (Figure 7 and Table S3c). There is also a negative correlation between dt and isotropic velocity changes ($c = -0.43$; $p < 0.0001$). Between 2007 and 2012, correlations at BOR between splitting parameters are still significant and in the same direction as those from 2000 to 2006 but are smaller ($c = 0.16$ for ϕ/dt and 0.25 for ϕ/ϕ_{in}; dt/ϕ_{in} remains relatively high at 0.31), suggesting either that the behavior was changed by the collapse or that including nonmultiplets dilutes the signals. After 2007, summit baseline increases (summit inflation) were only recorded during unrest periods (Figure 7).

Other permanent stations also yielded changes with time (Figure 7). At SNE on the northeastern side of the summit, changes in delay time between 2009 and 2011 are opposite those of BOR and are accompanied by rotation in the fast direction. SNE also has weak positive correlations between Vp/Vs and dt ($c = 0.14$). For the other stations, which are all on the base, we show the FERG-DERG baseline as representing pairs between the summit and the base, and we observe opposite behavior to the DSRG-SNEG summit baseline, with the FERG-DERG baseline decreasing when DSRG-SNEG increases and vice versa. Vp/Vs and dt at FER are anticorrelated during most of the time that the station was operational and are also anticorrelated with summit station BOR during 2007–2010. From 2008 through 2011, the changes in most of the measurements at base stations are slight.

3.2.2. Short-term Variation Linked to the October 2010 Eruption

The largest eruption sequence during the UnderVolc project occurred on 14 October 2010 [*Schmid*, 2011]. A seismic crisis and geodetic changes culminated in an eruption at the southern base of the central cone, near station FOR at 15:30 UT (Figure 1). The seismic crisis began at 09:45 UT on 14 October 2010 [*Roult et al.*, 2012] although earthquakes were present before then [*Schmid*, 2011]. Figure 8 shows the evolution over time of relocated earthquakes and seismic energy. Two multiplets, F01 (red in Figure 8c) and F02 (black in Figure 8c), are recognized, with F01 being further east than F02. F02 is in a confined region that does not

Figure 8. Evolution of seismicity over time on 14 October 2014. (a) Gray stars are locations of earthquakes in families F01 and F02 in terms of epicenters (top right) and depth (top left and bottom). Coordinates are Gauss-Laborde. Blue and black stars mark the locations of the blue and black waveforms discussed later and shown in Figure S4. (b–e) In all graphs, horizontal axis is in minutes since midnight (UT) on 14 October 2010. Red lines represent 10:00, 11:00, and 16:00. (b) Height of maximum seismic intensity in kilometers above sea level using the method of *Taisne et al.* [2011]. Between 730 and 930 min, the seismic intensity is too shallow to resolve. Gray circles represent the spread in the measurements. (c) Easting for F01 (red diamonds) and F02 (black diamonds). Blue diamonds are the blue earthquakes shown in Figure S4. (d) RMS amplitudes at stations UV05 (black) and UV11 (red) calculated for 10 min time windows in the 0.5–0.49 Hz frequency band. (e) Numbers of earthquakes in 4 min intervals.
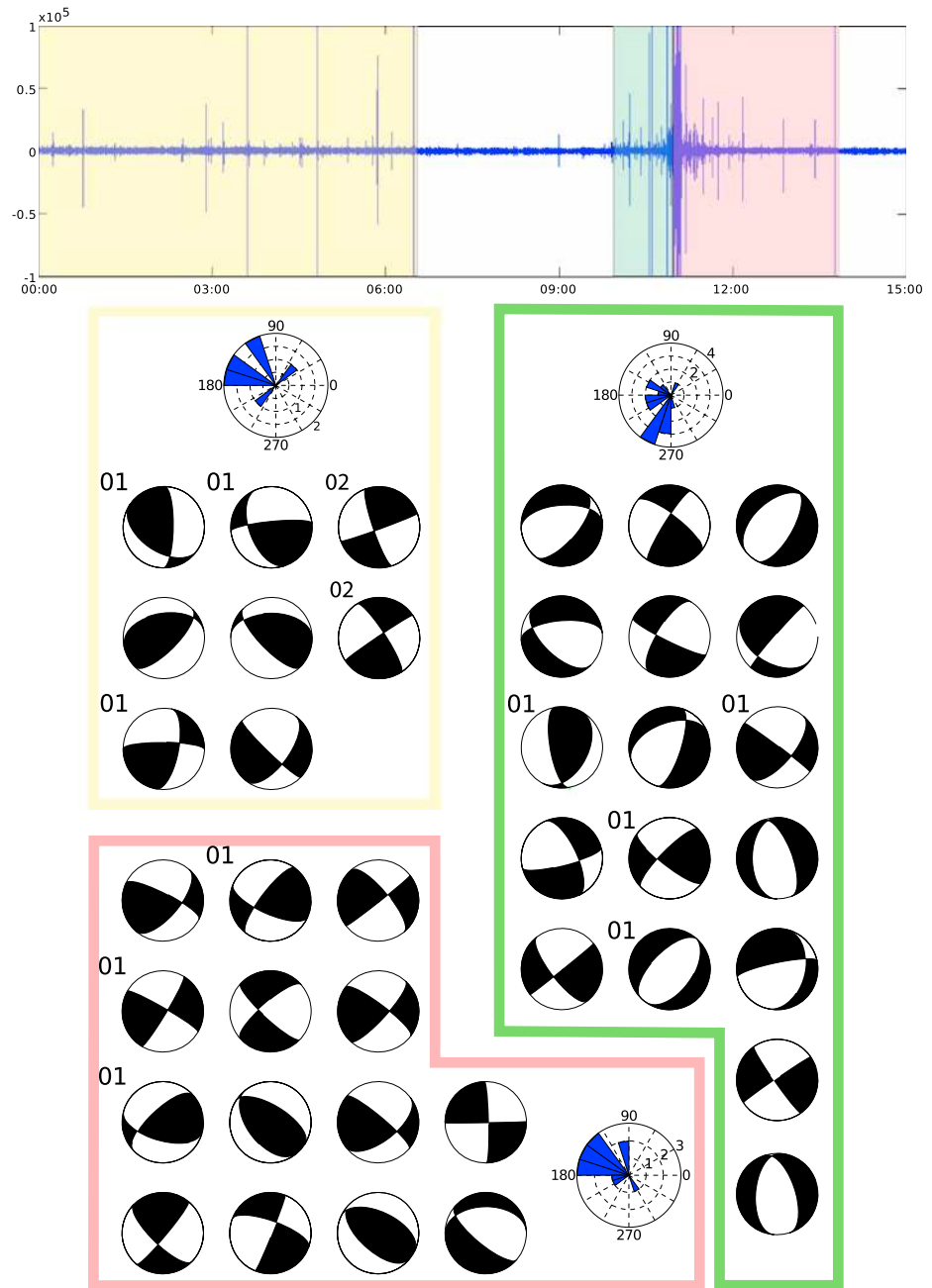
Figure 9. Focal mechanism changes with time before the 14 October 2010 eruption. The top panel shows the vertical seismogram from station FOR from times 00:00 to 15:00. The colors on the seismogram are coded to the boxes around the three groups of focal mechanisms. Rose diagrams represent rake angles. Earthquakes that belong to F01 and F02 are labeled. There are only two in F02, and they occur during the first period.

change between 09:00 and 11:00 and stops just before 11:00. Meanwhile, F01 has two stable eastings, with a third location that starts at 10:15 and migrates eastward until 11:00, with the migration discontinuing just after F02 ceases. After 11:00, most seismicity is in F01 and is at a single easting. Numbers and amplitudes of earthquakes are at a maximum between about 10:00 and 11:00. In addition to these earthquakes, which all occur near the same depth at sea level, dike propagation is accompanied by diffuse seismic energy release, which we locate by amplitude ratio analysis [*Taisne et al.*, 2011]. Figure 8b shows the height above sea level of the maximum seismic intensity (the surface is at 2.5 km above sea level). The height was fairly constant between 10:00 and 11:00 and then increased until about 12:00 when it reached the surface.
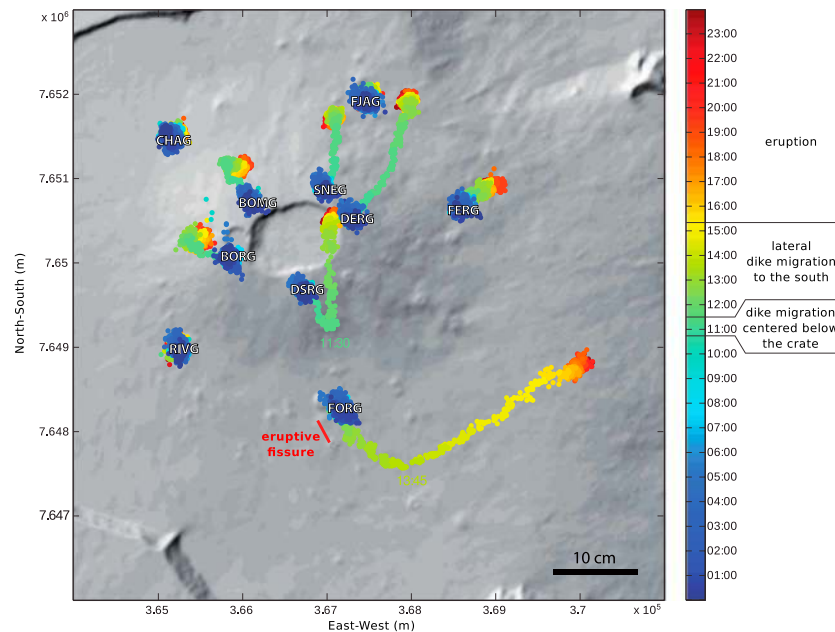
Figure 10. Position of geodetic stations as a function of time on 14 October 2010. Measurement at 00:00 is positioned at the average location of the station. Movements from those points are represented by displacements according to the scale in the lower right of the figure, colored by time. Key times of interest are noted.

Focal mechanisms for earthquakes during the eruption sequence have average rake angles that vary over three different time periods, independent of multiplet (Figure 9 and Table S4). First, there is a low-seismicity period (from 0:00 to 6:15) with mostly strike-slip-type events with a reverse component, with a positive rake angle, between 90° and 180° (see rose diagrams). From 10:00 to 11:00, we observe dominant normal faulting with most rakes between 180° and 270° (negative in Table S4). Finally, from 11:10 to 13:45, we again observe strike-slip-type events with a reverse component with slip vectors between 90° and 180° (Table S4). There were 386 shear wave splitting measurements from 39 earthquakes that had focal mechanisms determined. Correlations of focal mechanism parameters with location and splitting measurements for 14 October are shown in Table S5. Among these earthquakes, there was a positive correlation between rake and latitude ($c = 0.3$) and between longitude and both strike ($c = 0.2$) and dip ($c = 0.35$). Therefore, some of the time variation could be caused by a spatial variation.

As in previous eruptions, GPS and tilt signals varied strongly in time during dike propagation. Figure 10 shows changes in GPS observations as a function of time at stations that are within the Enclos Fouqué caldera. Starting at about 10:45, stations on the north rim of the central cone, SNEG and DERG, moved rapidly away from the crater (10–20 cm) and then stayed there. Stations somewhat west of the summit, BORG and BOMG, moved only about 5 cm further away from the volcano during the same time. DSRG on the southern rim started moving south (away from the crater) and reversed course at 11:30, indicating a migration of the pressure source to the south.

The GPS stations at the base of the central cone, to the north and west, CHAG, FJAG, and RIVG, stayed nearly constant. The only basal stations that moved were FORG, close to the eruptive fissures, and FERG, on the unstable eastern flank [*Staudacher and Peltier*, 2015]. FERG started to move slightly at 11:00 and continued moving until 13:00. FORG started moving later, at about 11:45, first southeast (oblique to the dike path), and changed course at about 13:45 to move northeast, perpendicular to the dike path. These data are being compared with seismic intensity data to model the propagation of the tip of the dike (B. Taisne et al., unpublished data, 2015). This approach is used because pressure concentration in the vicinity of the dike tip is causing deformation as well as rock breakage, producing seismic energy that is recorded by the network. Thus, the high concentration of stresses around the dike tip is approximated by a migrating Mogi source. Figures 11, S2, and S3 show 20-point moving medians of ϕ, dt, and Vp/Vs for stations with more than 40 measurements, along with GPS baselines between nearby stations. Including the entire sequence,
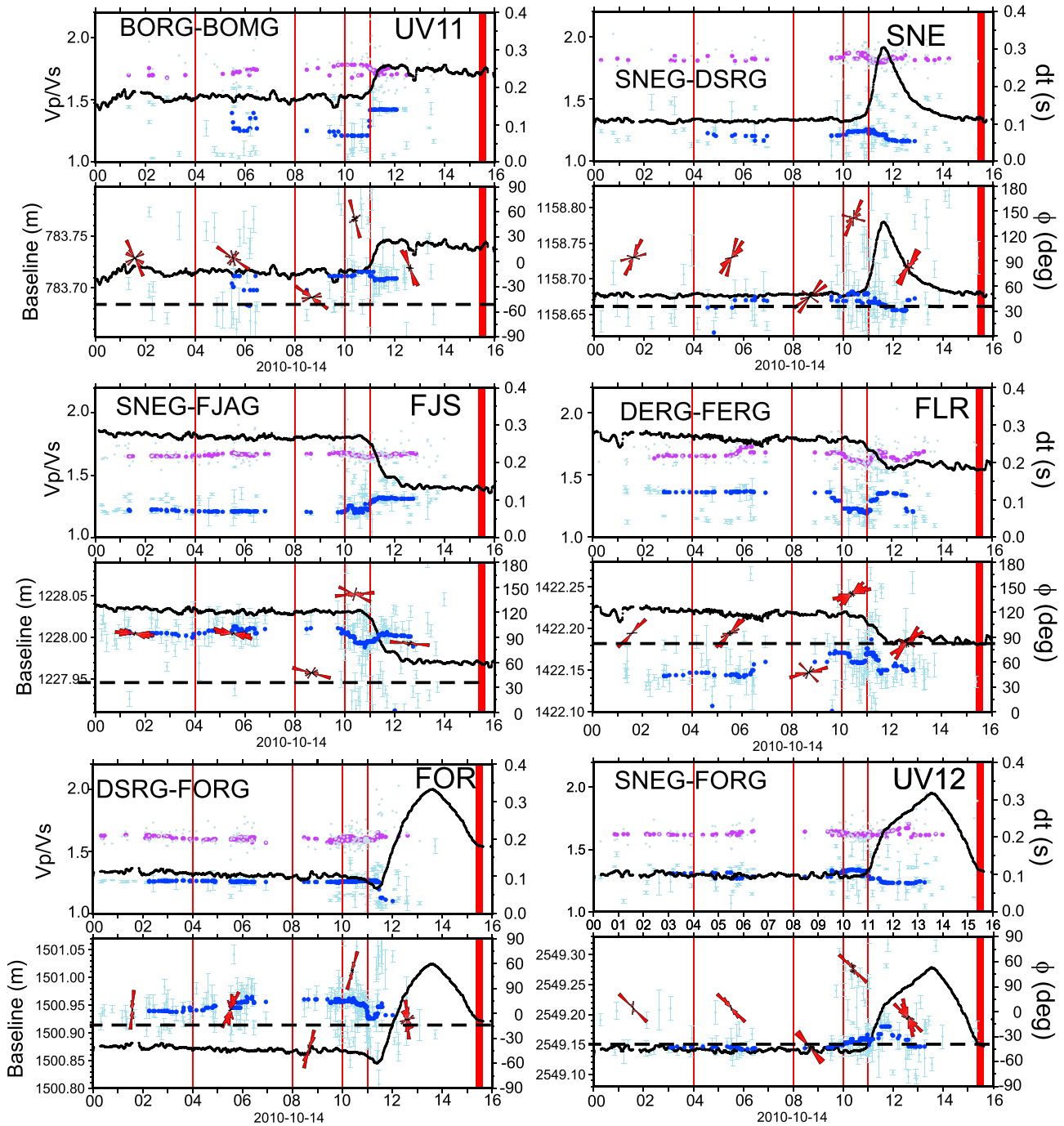
Figure 11. Shear wave splitting measurements and moving medians on 14 October 2014. Sky blue are individual measurements of ϕ or dt, and dark blue are 20-point moving medians. Vp/Vs ratio (light gray circles for individual points and purple circles for 20-point moving average) is shown on the dt plot, and GPS baseline (black lines) between nearby station pairs is shown. The time axis is in hours from the start of 14 October 2010. There are thin red lines marking the times bounding the rose diagrams. Lines between 10:00 and 11:00 bound the time of changed average focal mechanisms (green in Figure 9). The scale for the baseline on the left of the ϕ axis is the same as shown for that on dt above it. The dashed lines on the ϕ plots represent the azimuth from the station to the center of the Dolomieu crater. Here we show selected stations from the summit (UVV11 and SNE) and base stations (FJS, FLR, FOR, and UV12). The rest of the stations are shown in Figures S2 and S3.

250 earthquakes between 00:00 and 15:23 yielded shear wave splitting measurements. We retrieved 2000 AB quality measurements at 19 stations for the 4–10 Hz frequency band, of which 1679 fit the "emax > 3" criterion and 940 fit "emax > 5". Of the emax > 5 measurements, 238 were from Multiplet F01 and 184 were from Multiplet F02. The rest were in neither multiplet. We found little difference in parameters
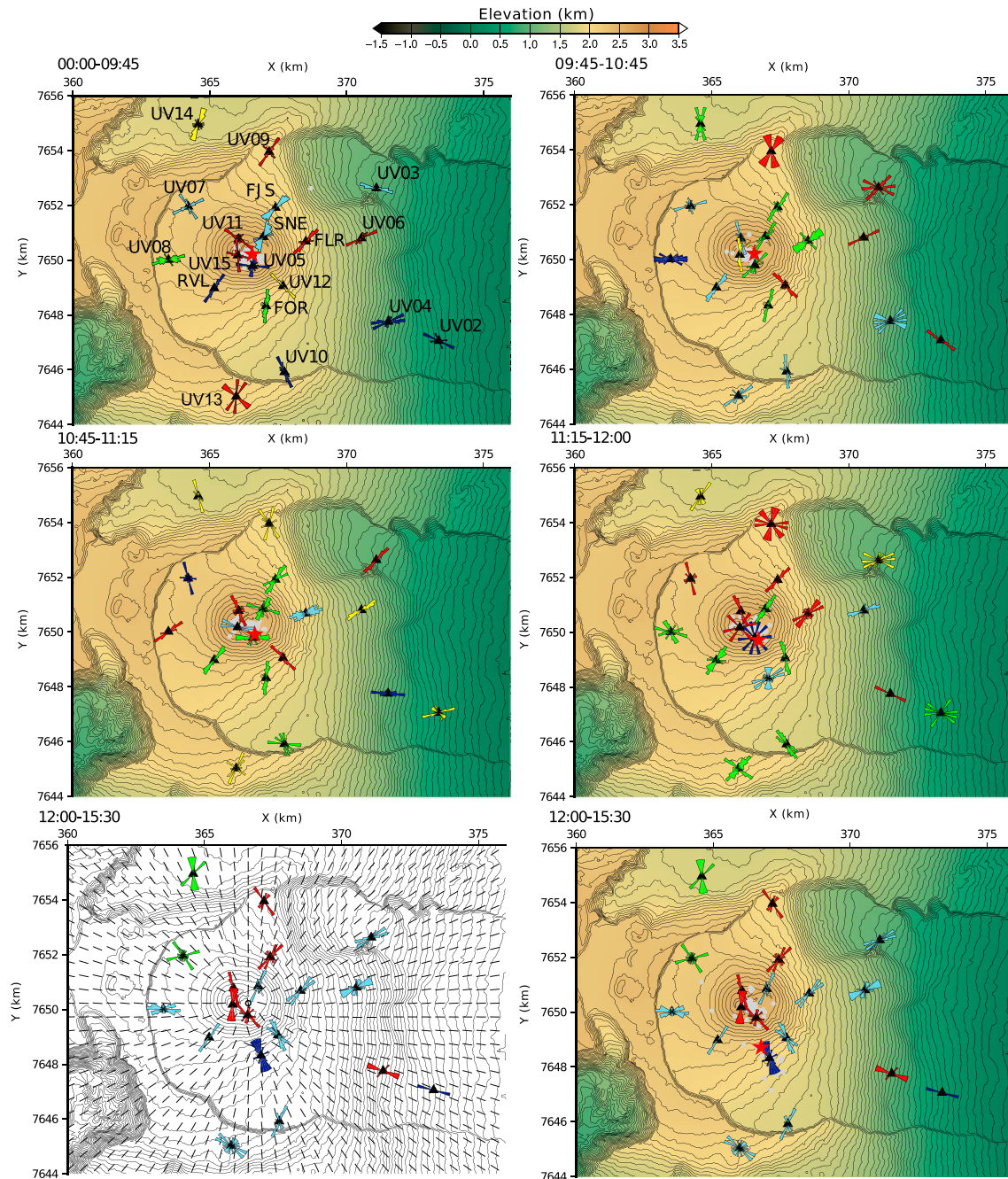
Figure 12. Maps with rose diagrams of ϕ for all measurements during the 14 October 2010 sequence. The time period represented is shown in the upper left corner above each plot. The basemap is a topographic map. Note that most of the stations are within the Enclos Fouqué caldera (delineated by the extremely close error contours; see Figure 1 for place names). The x and y coordinates are distances in Réseau Géodésique de la Réunion 1992 (RGR92) format, with distances measured in kilometers [*Reunion*, 2008]. Roses are colored by the average delay time for the measurements as in Figure 4a: 0.06–0.07: navy blue, 0.07–0.08: light blue, 0.08–0.09: green, 0.09–0.10: yellow, 0.10–0.11: orange, and 0.11–0.12: red. The red star is the average location of the propagating Mogi source calculated from an inversion of GPS and seismic intensity data during the time period shown. Bottom left corner shows the S_{Hmax} directions calculated from Coulomb 3.3 using two Mogi sources as discussed in the text and given in Table S6, for the last time period.

between those in Multiplet F01 and those in Multiplet F02 or those that do not belong to either multiplet, so we show all data together. To visualize time variations, we show results from emax > 3. We also show the data in map view for five time slices along with the modeled location of the dike tip (as a Mogi source) (from Taisne et al., unpublished data, 2015) (Figure 12).

At most stations, ϕ, dt, Vp/Vs, and GPS are relatively stable from 00:00 until 10:00 (Figures 11, 12, S2, and S3), with some stations exhibiting more than one population of measurements. At most of the stations, the largest changes in splitting parameters began at 10:45 when the geodetic changes began, and changes were concurrent in dt, ϕ, and Vp/Vs. As in the long-term study, Vp/Vs and delay times behaved differently between stations.

Compared to the early measurements, summit stations have better aligned ϕ (fewer double peaks in the rose diagrams) and less extreme variations in dt (reds and blues become yellows and greens) between 9:45 and 10:45 when the focal mechanisms are rotated (Figures 11 and 12). Only UV11 has a completely new population of ϕ during this period. After the focal mechanisms return to their original rakes and before the dike begins to migrate southward, from 10:45 to 11:15, ϕ at several summit stations (SNE, UV15, and UV05, almost directly under the source at this time) have stronger populations with E-W orientation. As the dike propagates southward between around 11:15–11:30 and 12:00, ϕ at UV15 and UV05 become variable. Finally, at the end of the sequence when the dike tip migrates to become situated nearly underneath station FOR, ϕ at the summit stations are oriented more N-S, pointing more toward the source.

Stations at the base of the cone (RVL, FOR, UV12, FLR, and FJS) maintain their average orientations until about 11:15–11:30, when the dike tip begins to move toward station FOR to the south. At this point, ϕ measurements become scattered at station FOR and rotate by about 45° at nearby station UV12. Average dt measurements at both FOR and UV12 decrease during this time. At RVL, ϕ measurements are somewhat scattered during the period, but dt measurements do not change significantly. FLR and FJS, further from the source, maintain fairly consistent directions but average dt increases. Finally, near the end of the cycle when the source is moving more southward, ϕ measurements for these base stations become better aligned and more consistent with previous values and the delay times generally decrease.

For stations further from the activity, at the edge of the caldera or on the eastern flank, there are fewer measurements due to the greater distance from the earthquakes, and the results are also more scattered over time (Figures S2 and S3).

At summit station UV11, increases in Vp/Vs are accompanied by decreases in dt and vice versa (Figures 11 and S4). The other summit stations do not show a strong relation between dt and Vp/Vs. Similar to UV11, base stations FJS, FOR, and UV12 have Vp/Vs increases when dt decreases. But at base station FLR, northeast of the summit, increases and decreases in dt are accompanied respectively by increases and decreases in Vp/Vs (Figure 11). Other stations were either ambiguous or did not have strong changes in one or both parameters (Figures 11, S2, and S3).

Increases in delay time were measured at most stations at some point during the time between 10:00 and 12:00 (some of the increases were either preceded or followed by decreases; Figures 11, 12, S2, and S3). Likewise, most stations had changes in ϕ during the geodetic disturbance. Most of the stations outside the summit region rotate to being more radial during the disturbance, while some stations near the estimated migrating dike tip rotate to being less radial during the disturbance. Supporting information Figure S4 shows detailed waveform evolution at station UV11.

4. Discussion

The most striking results from the shear wave splitting at PdF are that the average fast directions at most stations are roughly parallel to the azimuth between the station and the bottom of the central crater and that during eruption sequences there are substantial variations in ϕ and dt at the same times as changes in Vp/Vs, seismicity, isotropic velocity, geodetic positions, and eruptions. This correspondence is even present on an hourly basis as evidenced by the well-recorded eruption sequence on 14 October 2010. Changes in focal mechanisms were also observed during a 1 h period (10:00 to 11:00) just before the largest geodetic changes.

Traditionally, crustal shear wave splitting is considered to directly represent stress, with fast directions parallel to the orientation of vertically aligned cracks and hence to the maximum horizontal stress direction, and delay times representing a combination of crack density and path length [e.g., *Bianco et al.*, 2006; *Crampin*, 1994]. The distribution of magma sills and dikes could be a further source of anisotropy, since both geochemical and GPS data suggest that the post 2007 eruptions have been fed by shallow magma pockets [*Di Muro et al.*, 2014]. Dikes tend to fill cracks, so they will orient in the same direction as cracks.

Sills and horizontal cracks are expected to have less influence on shear wave splitting for vertically traveling waves. Changes in measured fast directions of up to 90° are considered to be evidence of rotation of stress directions [e.g., *Gerst and Savage*, 2004] or of "polarity flips" that are hypothesized to occur when stress gets high enough to locally reverse the fast polarization [*Bianco et al.*, 2006; *Zatsepin and Crampin*, 1997]. Observations of concurrent rotation of focal mechanism *P* axes and shear wave splitting fast directions at Soufriere Hills Volcano in Montserrat were consistent with the stress change hypothesis [*Roman et al.*, 2011]. Recently, changes in gas flux have also been suggested to cause polarity flips as well as changes in Vp/Vs ratios [*Johnson and Poland*, 2013]. At the depth range of our study, changes in Vp/Vs ratios could be caused by the relative proportion of liquids and gas in cracks [*Wang et al.*, 2012]. Low Vp/Vs ratios, such as the average values of 1.6 that we see on some of the stations, are often observed in geothermal and volcanic areas and are usually considered to be caused by pressurized gas-filled cracks [*Chatterjee et al.*, 1985; *Husen et al.*, 2004; *Unglert et al.*, 2011; *Vanorio et al.*, 2005]. Conversely, liquid-filled cracks can cause higher than average Vp/Vs ratios, above about 1.8 and higher [e.g., *Nur*, 1972; *Nur and Simmons*, 1969]. Changes in crack density can also cause changes in Vp/Vs ratios. Vp/Vs ratio increases with crack density in saturated media and decreases with crack density for gas-filled media [*Wang et al.*, 2012]. Therefore, changes in delay times that correlate negatively with Vp/Vs ratios may be considered to represent increasing numbers of pressurized gas-filled cracks [*Unglert et al.*, 2011]. Yet artifacts in shear wave splitting measurements and Vp/Vs ratios can occur. We consider average values, long-term variations, and short-term variations in terms of the possibility of artifacts and of interpretations of physical processes.

4.1. Average (Static) Values

4.1.1. Fast Polarizations

Through most of the region, ϕ are radial to the Dolomieu crater (Figure 4 and Table 1). Coseismic slip orientations just before the 2007 Dolomieu crater collapse, measured from focal mechanisms of event multiplets, were also radial to the center of the crater [*Massin et al.*, 2011]. This suggests that the fast directions are aligned with a compressional stress outward from the central summit, which is causing material to slip in a direction parallel to the compressional stress. Such a pattern is expected for a central magma plumbing system, which has provided the best long-term source to explain GPS data [*Staudacher and Peltier*, 2015] (1 in Figure 2), and is also consistent with the observed radial fissures (Figure 1b). Dikes have a somewhat more complicated stress pattern, and shallow dikes have been inferred for individual eruptive events [*Allard et al.*, 2011]. The presence of radially oriented fast directions and slip directions could also be explained by topographic stresses of the volcano. Mt. Fuji in Japan shows similar radially oriented fast directions, which have been modeled by the topographic stresses of the volcanic edifice [*Araragi et al.*, 2015]. Summit stations on the edge of the central cone have some ϕ measurements transverse to the central cone (Figure 4, stations SNE, UV05, and BOR), which is also parallel to fractures in the region (Figure 1b). These features can be explained by near-surface cracking or slumping, again due to gravitational forces.

Arrivals outside the shear wave window or conversions from *S* to *P* waves below a station could result in *P* waves being measured instead of *S* waves, which would yield apparent fast directions that are parallel to the earthquake station path. Since most earthquakes are immediately below the Dolomieu crater, that artifact would also result in the fast directions appearing radial to the center of the Dolomieu crater, which we have attributed to radial cracks. To test this possibility, we examined a restricted set of data in which the earthquake hypocenters were most nearly directly below the stations (straight-line angles of incidence < 45°) and so less likely to have conversions. For the 11 stations with more than 10 such measurements, only one (FOR) had a difference (−11°) of more than 6° between the average ϕ for the whole data set and the restricted data set. The lack of significant correlation between back azimuth and fast direction (Table S3) also suggests such artifacts are unlikely. Finally, examination of waveforms shows that the dominant energy for the records used for emax > 5 measurements is on the horizontal components, and therefore, the splitting is not being affected by converted phases. Therefore, we conclude that the radial fast directions are caused by cracks or stress, not by measurement artifacts.

4.1.2. Delay Times

Delay times can be used to determine crack densities. Crack density ρ is defined [*Hudson*, 1981] as the number of (idealized thin penny-shaped) cracks M times the cube of the crack radius a divided by the volume $\rho = M(a^3/V)$. It can be calculated from the delay time and the average shear wave velocity Vs using

Hudson's equation: $\rho = 7dt\text{Vs}/(8L)$, where dt is the time delay, Vs is the velocity, and L is the path length. Likewise the fractional velocity ratio can be calculated from $dt/L = (v_2 - v_1)/v_2 \times v_1$ where v_1 and v_2 are the fast and slow velocities. If $v_1 \sim v_2 = \text{Vs}$, then it reduces to

$$dt/L = \text{vfrac}/\text{Vs} \tag{1}$$

where vfrac is the fractional anisotropy and Vs is the average velocity. The median value for delay time divided by path length is 0.081 s/km, and the median path length is 1.8 km. Using Vs = 2.2 km/s for the average S velocity above sea level and for v_2 (Table S1) yields a fractional velocity ratio of 0.18 (18% anisotropy) and a crack density of 0.16, which are at the high end even for shallow volcanic regions, suggesting material near failure [*Crampin*, 1994]. This is reasonable considering the 2007 collapse represented such a failure. It is also consistent with the low magnitudes of earthquakes (<2.5).

However, delay times do not correlate well with distance ($c = 0.08$) (Table S3), suggesting that anisotropy may be strongest near the stations or that some other factor is affecting the delay time measurements. The least squares linear regression between the parameters is $dt = 0.08 + 0.0016 \times \text{distance}$. Using equation (1), the slope of 0.0016 s/km suggests anisotropy of only 0.3%.

The correlations between variables are not strong. One complicating factor is that there are different timescales for the different processes of change. *Schmid et al.* [2012] show that changes in parameters happen earlier before eruptions for some variables than for others. This difference will serve to dampen any correlations between the parameters. Nevertheless, regressions can help us to understand the rough scaling between parameters.

A linear regression between isotropic velocity change and relative delay time (dt divided by travel time T) dt/T at station BOR over the entire period yields

$$(dV/V) = -0.208 \times (dt/T) + 0.003 (\text{correlation coefficient } (c) = -0.211, \ p = 0.00000041) \tag{2}$$

Thus, a 1% increase in velocity corresponds to a fractional change of 0.21, or 21%, decrease in shear wave splitting. If both dV/V and dt are caused by cracks and the relationship is linear, then a 1% change in velocity corresponds to 21% of 0.16 or a crack density change of 0.034.

For GPS, we get

$$\text{GPS baseline length} = -2.81 \times dt + 1281.7 \ (c = -0.35, \ p < 0.0001) \tag{3}$$

that is, for an increase in baseline length of 0.01 m, dt changes by -0.03 s.

For comparison, for velocity compared to GPS, we get

$$\text{Baseline length} = 0.886 \times dV/V + 1280.5 (c = 0.57, \ p < 0.0001)$$

that is, for an increase in baseline length of 0.01 m, velocity increases by 0.009%.

The positive correlation of baseline length with velocity and negative correlation between baseline length and delay time in the long run (Table S3) are apparent in the general average increase in baseline between 2004 and 2007 with an average decrease in delay time (Figures 5a, 5c, and S1) and the overall increase in baseline and decrease in dt from mid-2007 to 2012 (Figures 7 and S1). It can be explained if increasing baseline length corresponds to greater compressional stress closing cracks, which increases isotropic velocity and decreases delay times.

4.1.3. Vp/Vs Ratios

Mean values of Vp/Vs ratio of 1.74 ± 0.09 are within the error of the average Vp/Vs of 1.75 assumed in the earthquake location model (Table S1 and Figure 4). However, the stations at the base of the central cone have low Vp/Vs (<1.70), suggesting a high concentration of gasses below the flank, and the stations on the summit have higher values; three of them (BOR, SNE, and UV05) have Vp/Vs > 1.8, suggesting a high proportion of liquids below the summit. These differences are measured both in the overall time period and in the largest events from the 2010 sequence. The weak positive correlations between Vp/Vs and dt at summit stations BOR and SNE ($c = 0.14; \ p < 0.01$) (Figure 7 and Table S3) could be interpreted as increasing numbers of fluid-filled cracks causing increasing delay time and Vp/Vs ratios. Except for station FJS, stations at the base generally have negative correlations between Vp/Vs and dt, as has been postulated to occur for gas-filled cracks [*Unglert et al.*, 2011].

Changes in incidence angle with respect to the crack plane can also result in apparent Vp/Vs ratio changes in cracked media [*Wang et al.*, 2012]. However, as we discuss above, the crack planes are probably vertical and oriented radial to the cone, so that the earthquake raypaths are near parallel to the crack fabric for both cone and flank stations, which should result in similar apparent Vp/Vs ratios.

Artifacts in Vp/Vs ratio calculations can come from errors in the earthquake origin time, upon which the calculations depend. When both P and S arrivals are available, errors in origin time tend to give rise to errors in depth [*Shearer*, 2009]. Since most studies of the earthquake clusters used have suggested that depths are fairly constant, we consider that a correlation between Vp/Vs and hypocentral parameters at close groups of stations could be caused by measurement artifacts. For long-term variations at summit stations, Vp/Vs is correlated negatively with depth at BOR ($c = -0.253$) and SNE ($c = -0.529$), but for base stations, Vp/Vs is not correlated with depth (FER ($c = 0.0076$), FJS ($c = 0.067$), RVL ($c = 0.125$), FOR ($c = 0.14$)).

For the 14 October 2010 period, higher station numbers and cross-correlations resulted in better earthquake depths, yet the difference in Vp/Vs between summit and base stations is still apparent. Earthquakes with focal mechanisms are considered since they are the largest and best recorded. For summit stations, Vp/Vs $= 1.8 \pm 0.02$ and it is uncorrelated with depth ($c = 0.02$; $p = 0.88$); here Vp/Vs is correlated most strongly with distance and with parameters relating to the errors (e.g., for Vp/Vs versus SNR, $c = -0.36$, $p = 0.005$). For base stations, Vp/Vs $= 1.622 \pm 0.005$ and it is also not well correlated with depth ($c = -0.13$; $p = 0.15$), but it is again somewhat correlated with distance ($c = 0.23$; $p = 0.0082$) and again with errors (for SNR, $c = -0.21$; $p = 0.016$). So, in both studies, there is some correlation of Vp/Vs with location, but the lack of correlation with depth for the best located summit earthquakes suggests that the spatial differences in Vp/Vs are likely to be real.

There is (weak) surface evidence of water-rich vapor discharge and weak thermal anomalies at the volcano summit [*Di Muro et al.*, 2012, 2014; *Staudacher*, 2010], and no surface evidence of fluid release at the volcano base. A self-potential study [*Barde-Cabusson et al.*, 2012] suggests that the central craters and the rift zones correspond to preferential pathways of hydrothermal fluid ascent, while downward infiltration of cold fluids and groundwater can occur on the volcano flanks. We suggest that the gas underneath the summit stations is readily released so that cracks are dominantly liquid filled, causing high Vp/Vs ratios. This could be accomplished by the earthquakes creating fluid pathways in the gray region in Figure 2 and may also be related to the multiple collapse events that have affected the volcano summit [*Roult et al.*, 2012] and the very high density of concentric fissures surrounding the summit crater (Figure 1b). Beneath the base of the volcano, there are fewer earthquakes to open up fluid pathways to the surface (white regions in Figure 2), so gasses may be trapped and remain at high pressure so that they are not observed at the surface and cause low Vp/Vs ratios at the volcano base.

4.2. Long-Term Time Variations and Station-Specific Correlations

We consider that the increase in delays before eruptions are caused by increasing crack densities, much like the decrease in surface wave speeds from ambient noise analysis is attributed to crack densities increasing just before the eruptions [*Brenguier et al.*, 2008]. The negative correlation between delay times and isotropic velocity supports this.

There is a marked change in the behavior of the volcano before and after the 2007 eruption. The increase of crack density before eruptions between 2000 and 2007 can be directly linked to the pre-eruptive summit inflation [*Peltier et al.*, 2009a] and indicates that increases in GPS baseline lengths occur alongside (and possibly due to) increases in crack density, causing both decreasing wave speeds and increasing delay times (Figure 5a). Similar behavior of increasing GPS baseline length with increasing delay times was observed at Asama volcano in Japan during dike inflation [*Savage et al.*, 2010b]. At BOR, the general increase in GPS baseline and Vp/Vs, before 2007 (Figure S1 and Table S3) may reflect the gradual increase in liquid-filled crack density and size during the preparation period before the Dolomieu collapse, but delay times do not exhibit as strong an increase.

The changes in geophysical signatures on and after April 2007 are all consistent with the crater collapse (Figures 5 and 7). The collapse leads to motion of the summit stations toward the Dolomieu center (summit deflation), which leads to elongation of the flank of the cone (baselines increase between summit and base stations; e.g., FERG-DERG) whereas the summit deflates (baseline decrease across summit stations, e.g., DSRG-SNEG) [*Peltier et al.*, 2015]. Sharp increases in dt at summit station BOR and decreased

isotropic velocity in the region are consistent with increased rock damage (and therefore crack density) from the disruption. At base station FER, dt increased right before the collapse as cracks were starting to form but returned to normal right after the collapse. At both summit station BOR and base station FER, ϕ rotates to be less radially aligned at the time of the collapse, probably due to the disturbance in the stress field from the change in the system.

xDuring intereruptive periods after 2007, summit baselines and dt at summit station BOR as well as base station FER decrease and isotropic velocity increases, probably due to crack healing (Figure 7). When it was operating, SNE, which is also located on the summit, behaved like BOR in terms of Vp/Vs and delay time changes (Figure 7), suggesting similar mechanisms. FOR, FJS, and RVL, all at the base of the cone, behave less alike, possibly because of different vents being active at different times [e.g., *Peltier et al.*, 2009a; *Roult et al.*, 2012].

The evolution of ϕ over time suggests either that the crack populations rotate in response to a rapid reorientation of the stress direction when the dike/magma chamber is inflated or that there is a rapid variation in overpressure [*Johnson and Poland*, 2013; *Zatsepin and Crampin*, 1997].

4.3. The 14 October 2010 eruption sequence

As discussed above in section 4.1, the presence of radially oriented fast directions could be explained either by gravitational stresses due to the topography of the volcano or by inflating magma bodies beneath the volcano or both. The 14 October eruptions suggest that at least some of the stress is caused by the inflating magma body, because the geodetic observations (Figure 10) have the most central stations start moving away from the crater at 10:45, the same time as the fast directions are becoming more radial to the crater (Figures 11, 12, S2, and S3). Radial changes can be explained by disturbances from the rising dike that changes the local stress in its vicinity. The dike propagates vertically below the summit just before its propagation to the southern flank toward station FOR (Figures 8 and 10; see also Taisne et al., unpublished data, 2015).

4.3.1. Splitting Measurements

The map views of time slices (Figure 12) and the moving medians of parameters with time (Figures 11, S2, and S3) show that rapid time variations are occurring. A simple model shows that in principle changes in stress from the dike propagation may be explained by the movement of a magmatic source combined with a background radial stress field that could be due to gravitational or previously accumulated magmatic sources (Figure 12, S5, and S6). Although vertical stresses are opposite for a gravitational source compared to a magmatic (i.e., Mogi) source beneath the summit, the horizontal forces in both cases are radial and so we approximate the radial stresses by a Mogi source under the volcano summit. As an illustration, we use the Coulomb 3.3 code [*Lin and Stein*, 2004; *Toda et al.*, 2005] to calculate the maximum horizontal stress direction for two Mogi sources of different sizes and relative positions (see Table S6 for source values). The larger source situated beneath the Dolomieu crater represents a combination of deeper long-term magma chamber inflation with gravitational forces due to topography. The second, smaller source, is modeled based on dike propagation, approximated by a series of propagating Mogi sources as determined by Taisne et al. (unpublished data, 2015), which move from under the crater to under station FOR through the time period. Because the dominant source is the one under the crater, SHmax is radial to the crater for most stations except those nearest the smaller source. Figures S5 and S6 show examples of propagating Mogi sources in different time slices and a dike source. Full modeling is beyond the scope of this paper.

The change in the rake of the focal mechanisms (Figure 9 and Table S4) from dominantly strike slip/reverse to dominantly strike slip/normal occurred between 10:00 and 11:10, during the time of maximum seismicity rate and energy release (Figure 8), but just before the time of the rapid changes in fast directions and the rapid GPS movements (Figure 10) and the movement of seismic intensity toward the surface (Figure 8). The group of earthquakes analyzed for focal mechanisms included earthquakes from both families F01 and F02 and those not associated with either family. All time periods included F01 and nonassociated earthquakes; there were only two events from F02, and they occurred in the first time period (Figure 9), so the focal mechanism changes were not caused by different families.

The change from oblique reverse to oblique normal faulting during the hour prior to the major GPS movement could be caused by changing stresses at the depths of the earthquakes just before the

migration of the dike ($S_1 > S_2 \sim S_3$ for the oblique reverse mechanisms and $S_1 \sim S_2 > S_3$, with S_2 vertical for dominant strike-slip mechanisms, where S_1, S_2, and S_3 represent maximum, intermediate, and minimum principal stresses, respectively). Earthquakes with oblique normal-faulting mechanisms are surrounded by others with oblique reverse mechanisms (Figure 3b), so it is unlikely that the difference is due to earthquakes moving during this time. A buildup of stress just prior to the dike propagation might explain the increased delay times during this time period (Figure 12) as well as the small rotation in ϕ at summit stations.

4.3.2. Focal Mechanisms and Initial Polarizations

Changes in focal mechanism will change the initial polarizations of the S waves, and a change in initial polarization can cause variations in apparent shear wave splitting parameters, particularly if there is more than one anisotropic region encountered along the raypath [*Silver and Savage*, 1994]. Thus, the change in splitting parameters from 10:00 to 11:00 could be due to the same change in stress or to a change in the character of the S arrivals as the focal mechanisms changed. However, the changes in S polarization calculated from the changes in focal mechanisms were not systematic at any stations and were not strongly correlated with any other variables (Table S5). Since the initial polarizations determined from the splitting code, ϕ_{in}, are not correlated with those expected from the focal mechanisms, there must be something else affecting the measurements. There could be several layers of anisotropy, or there could be scattered arrivals affecting the measurements of ϕ_{in} and causing the cycle skipping discussed below. In a system with two layers of anisotropy, the waveform will be split first by the lower layer and again by the upper layer. If the delay time in the lower layer is more than a wave period, then ϕ_{in} determined by the splitting code should be the fast direction of the lower layer. However, if it is less than a period, the measured fast directions and delay times will be a nonlinear combination of the two directions [*Silver and Savage*, 1994] and it is likely that the measured ϕ_{in} will be wrong. If the fast direction in the lower layer varies, then the nonlinear effects will occur and changes in all measured parameters are likely. Moreover, scattering would also be expected to vary because there are different amplitudes coming from different directions.

The correlations can help to determine if the results contain measurement artifacts. For example, there has been some suggestions that measured delay times may be caused not by true time delays but by scattered waves arriving after the initial arrival [*Aster et al.*, 1990]. In this case, there could be a few possible artifacts:

1. If the medium were isotropic, then the initial polarization of the wave would arrive first, with scattered waves coming later; then the measured fast direction would be equal to the calculated polarization from the focal mechanism. These two parameters do not have significant correlation (Table S5). Therefore, we do not think this is happening on a widespread basis.
2. If an *S-P* conversion occurred, then the apparent fast polarization measured would be equal to the event station back azimuth. As discussed above, this is not occurring.
3. If the medium were anisotropic, the fast polarization might be measured correctly but the delay time could be incorrect. The calculated incoming polarization would probably also be wrong. This could in fact explain the lack of correlation between the calculated and measured incoming polarizations and the lack of strong increase in delay time with distance.

4.4. Cycle Skipping

Several lines of evidence suggest that cycle skipping is affecting the data. The classic example of cycle skipping is for sine waves: if two sine waves are separated by a whole period, they will appear exactly the same, and a split wave with several cycles can have fast directions and slow directions switched, with multiples of one-half period difference between the two sets of delay times [e.g., *Matcham et al.*, 2000]. The fast directions at BOR both within and between each multiplet during 2000–2006 vary by a large amount, with moving medians between 30° and 120° and delay times that also vary with jumps over time (Figures 5a and 5c).

Recently, *Walsh* [2012] used the repeating earthquakes in Multiplet 01 at BOR to show that cycle skipping can be more complicated, with changes in calculated incoming polarization direction ϕ_{in} appearing with delay time differences of one-half cycle [*Walsh*, 2012]. This cycle-skipping phenomenon is investigated in greater detail using synthetic seismograms, in another paper in this volume [*Castellazzi et al.*, 2015]. Such effects explain the observed waveforms as well as the rapid jumps in delay times and fast directions at some multiplets at station BOR. It is supported by a relatively strong correlation between *dt* and ϕ_{in} of *c* = 0.26 at the other stations during the 14 October eruption. The delay time increases within individual multiplets at station BOR

are mostly caused by several populations of measurements with discrete delay times and polarizations (Figures 5 and 6). The populations with larger delay times tend to increase over time at the expense of those with smaller delay times so that the average increases. This leads to jumps in moving medians. However, a smoothly varying stress should cause slowly increasing time delays, with "stretched" waveforms, as seen in other studies of splitting or velocity changes [*Bokelmann and Harjes*, 2000; *Li et al.*, 1998].

While cycle skipping is clearly occurring in the multiplets at station BOR, it is also clear that the process is not random. The numbers of events yielding measurements of each type of cycle changes systematically over time. Possible explanations are that scatterers in the medium are changing over time or that the raypaths are varying spatially over time. The dependence of latitude, longitude, and depth with time means that path changes cannot be ruled out. A comprehensive numerical analysis of the effect of scatterers is planned to try to understand this phenomenon.

4.5. Spatial Variations Versus Path Properties Changing

Crustal shear wave splitting parameters vary widely for nearby stations both generally and specifically here (Figure 4), and so spatial variations in anisotropy can be combined with earthquake source location changes to yield apparent time variations in anisotropy. This may be affecting some of the data because of the strong variation of earthquake location and depth with time discussed above under correlations. However, the changes on 14 October occur the same way regardless of whether we are looking at F01, F02, or the remaining events and regardless of whether we look at the highest- or medium-quality measurements. This suggests they are real and not simply due to changing paths, even though cycle skipping is also occurring as discussed above.

5. Conclusions

At Piton de la Fournaise, shear wave splitting measurements indicate that the fast direction of anisotropy is radially oriented to the central cone, Vp/Vs is large under the summit and small at the base of the cone, and measured parameters vary along with several other geophysical measurements associated with volcanic activity. Implications are as follows:

1. Focal mechanisms [*Massin et al.*, 2011] and fast directions suggest compressional stress is perpendicular to the central cone, causing cracks to align radially to the crater. While there could also be some contribution from gravitational stresses, changes in fast direction during eruption sequences suggest that stress changes caused by magma intrusions are a strong factor.
2. The variation of *dt* with time is consistent with isotropic velocity variations [*Brenguier et al.*, 2008; *Rivet et al.*, 2014] with increasing numbers of cracks before the eruptions formed in response to an inflating source in depth [*Peltier et al.*, 2009a]. A qualitative comparison of the splitting changes with time leading up to the 14 October 2010 eruption is consistent with that from propagating Mogi sources representing a moving dike tip, combined with a background radial stress field from gravitation or buried magmatic intrusions.
3. Low Vp/Vs ratios at the base of the summit cone indicate accumulating gas in pore space, and high ratios at the volcano summit suggest fluid-filled cracks. As illustrated in Figure 2, gas may be being released from a cooling intrusive magma complex (blue area labeled 5). The gas directly under the summit may be released to the surface through pathways broken by the seismicity in the gray regions, leaving mainly fluid-filled cracks. Conversely, the base of the volcano lies above an area with few earthquakes (white regions), so that there may be fewer paths for the gas to escape, leaving gas-filled cracks under the flanks.
4. Measurements made on multiplets suggest that cycle skipping is affecting the shear wave splitting measurements, and interference with scattered waves may also affect the results. However, systematic changes over time suggest that the averages provide useful, physically interpretable outcomes. A comprehensive analysis of the effects of scattering on shear wave splitting measurements and their averages is warranted.

References

Allard, P., A. La Spina, G. Tamburello, A. Aiuppa, A. Coquet, F. Brenguier, D. Coppola, A. Di Muro, M. Burton, and T. Staudacher (2011), First cross-correlated measurements of magma dynamics and degassing during a dyke eruption at Piton de la Fournaise hot spot volcano, Reunion Island, Abstract V22A-04 presented at 2011 Fall Meeting, AGU, San Francisco, Calif.
Araragi, K. R., M. K. Savage, T. Ohminato, and Y. Aoki (2015), Seismic anisotropy of the upper crust around Mount Fuji, Japan, *J. Geophys. Res. Solid Earth*, *120*, doi:10.1002/2014JB011554.

Aster, R. C., P. M. Shearer, and J. Berger (1990), Quantitative measurements of shear wave polarizations at the Anza seismic network, southern California: Implications for shear wave splitting and earthquake prediction, *J. Geophys. Res.*, *95*(B8), 12,449–12,473, doi:10.1029/JB095iB08p12449.

Babuska, V., and M. Cara (1991), *Seismic Anisotropy in the Earth*, 217 pp., Kluwer Acad., Dordrecht, Netherlands.

Bachèlery, P. (1981), Le Piton de la Fournaise (île de la Réunion) étude volcanologique, structurale et pétrologique, Université de Clermont-Ferrand II, Clermont-Ferrand, France.

Barde-Cabusson, S., et al. (2012), Structural control of collapse events inferred by self-potential mapping on the Piton de la Fournaise volcano (La Réunion Island), *J. Volcanol. Geotherm. Res.*, *209–210*, 9–18, doi:10.1016/j.jvolgeores.2011.09.014.

Barth, A., F. Wenzel, and D. Giardini (2007), Frequency sensitive moment tensor inversion for light to moderate magnitude earthquakes in eastern Africa, *Geophys. Res. Lett.*, *34*, L15302, doi:10.1029/2007GL030359.

Battaglia, J., and F. Brenguier (2011), Seismogenic structures activated during the pre-eruptive and intrusive swarms of Piton de la Fournaise volcano (La Réunion island) between 2008 and 2011, Abstract S31B-2232 presented at 2011 Fall AGU Meeting, AGU, San Francisco, Calif., 5-9 Dec.

Berens, P. (2009), CircStat: A MATLAB toolbox for circular statistics, *J. Stat. Software*, *31*(10) 1–21.

Bernard, A., and M. Munschy (2000), Le bassin des Mascareignes et le bassin de Laxmi (océan Indien occidental) se sont-ils formés à l'axe d'un même centre d'expansion ?, *C. R. Acad. Sci. Ser. IIa: Earth Planet. Sci.*, *330*(11), 777–783, doi:10.1016/S1251-8050(00)00221-4.

Bianco, F., L. Scarfi, E. D. Pezzo, and D. Patane (2006), Shear wave splitting changes associated with the 2001 volcanic eruption on Mt. Etna, *Geophys. J. Int.*, doi:10.1111/j.1365-246X.2006.03152.x.

Bokelmann, H. R. G., and H.-P. Harjes (2000), Evidence for temporal variation of seismic velocity within the upper continental crust, *J. Geophys. Res.*, *105*(B10), 23,879–23,894, doi:10.1029/2000JB900207.

Booth, D. C., and S. Crampin (1985), Shear-wave polarizations on a curved wavefront at an isotropic free surface, *Geophys. J. R. Astron. Soc.*, *83*, 31–45.

Brenguier, F. (2012), First results from the UnderVolc high resolution seismic and GPS network deployed on Piton de la Fournaise volcano, *Seismol. Res. Lett.*, *83*(1), 97–102, doi:10.1785/gssrl.83.1.97.

Brenguier, F., N. M. Shapiro, M. Campillo, A. Nercessian, and V. Ferrazzini (2007), 3-D surface wave tomography of the Piton de la Fournaise volcano using seismic noise correlations, *Geophys. Res. Lett.*, *34*, L02305, doi:10.1029/2006GL028586.

Brenguier, F., N. M. Shapiro, M. Campillo, V. Ferrazzini, Z. Duputel, O. Coutant, and A. Nercessian (2008), Towards forecasting volcanic eruptions using seismic noise, *Nat. Geosci.*, *1*, 126–130, doi:10.1038/ngeo104.

Brenguier, F., D. Clarke, Y. Aoki, N. M. Shapiro, M. Campillo, and V. Ferrazzini (2011), Monitoring volcanoes using seismic noise correlations, *C. R. Geosci.*, *343*, 633–638, doi:10.1016/j.crte.2010.12.010.

Castellazzi, C., M. K. Savage, E. Walsh, and R. Arnold (2015), Shear-wave automatic picking and splitting measurement at Ruapehu volcano, New Zealand, *J. Geophys. Res. Solid Earth*, *120*, doi:10.1002/2014JB011585.

Chatterjee, S., A. Pitt, and H. Iyer (1985), Vp/Vs ratios in the Yellowstone National Park region, Wyoming, *J. Volcanol. Geotherm. Res.*, *26*(3–4), 2113–2230, doi:10.1016/0377-0273(85)90057-5.

Clarke, D., L. Zaccarelli, N. M. Shapiro, and F. Brenguier (2011), Assessment of resolution and accuracy of the moving window cross spectral technique for monitoring crustal temporal variations using ambient seismic noise, *Geophys. J. Int.*, *186*(2), 867–882, doi:10.1111/j.1365-246X.2011.05074.x.

Clarke, D., F. Brenguier, J.-L. Froger, N. M. Shapiro, A. Peltier, and T. Staudacher (2013), Timing of a large volcanic flank movement at Piton de la Fournaise Volcano using noise-based seismic monitoring and ground deformation measurements, *Geophys. J. Int.*, *195*, 1132–1140, doi:10.1093/gji/ggt276.

Crampin, S. (1994), The fracture criticality of crustal rocks, *Geophys. J. Int.*, *118*, 428–438.

Di Muro, A., A. Aiuppa, M. Burton, N. Metrich, P. Allard, T. Fougeroux, G. Giudice, and R. Guida (2012), Intra-eruptive gas emissions and shallow magma storage after the 2007 summit caldera collapse of Piton de la Fournaise, Reunion Island, paper presented at EGU, Vienna.

Di Muro, A., N. Metrich, D. Vergani, M. Rose, P. Armienti, T. Fougeroux, E. Deloule, L. Arienzo, and L. Civetta (2014), The shallow plumbing system of Piton de la Fournaise Volcano (La Reunion Island, Indian Ocean) revealed by the major 2007 caldera-forming eruption, *J. Petrol.*, *55*(7), 1287–1315, doi:10.1093/petrology/egu025.

Duncan, R. A., J. Backman, and L. Peterson (1989), Reunion hotspot activity through tertiary time: Initial results from the ocean drilling program, leg 115, *J. Volcanol. Geotherm. Res.*, *36*(1–3), 193–198, doi:10.1016/0377-0273(89)90013-9.

Fontaine, F. R., G. Roult, L. Michon, G. Barruol, and A. Di Muro (2014), The 2007 eruptions and caldera collapse of the Piton de la Fournaise volcano (La Reunion Island) from tilt analysis at a single very broadband seismic station, *Geophys. Res. Lett.*, *41*, 2803–2811, doi:10.1002/2014GL059691.

Geller, R. J., and C. S. Mueller (1980), Four similar earthquakes in central California, *Geophys. Res. Lett.*, *7*(10), 821–824.

Gerst, A. (2003), Temporal changes in seismic anisotropy as a new eruption forecasting tool?, MS thesis, pp. 184, Victoria Univ. of Wellington, Wellington.

Gerst, A., and M. K. Savage (2004), Seismic anisotropy beneath Ruapehu Volcano: A possible eruption forecasting tool, *Science*, *306*, 1543–1547.

Got, J. L., J. Frechet, and F. W. Klein (1994), Deep fault plane geometry inferred from multiplet relative relocation beneath the south flank of Kilauea, *J. Geophys. Res.*, *99*(B8), 15,375–15,386, doi:10.1029/94JB00577.

Got, J., A. Peltier, T. Staudacher, P. Kowalski, and P. Boissier (2013), Edifice strength and magma transfer modulation at Piton de la Fournaise volcano, *J. Geophys. Res. Solid Earth*, *118*, 1–18, doi:10.1002/jgrb.50350.

Got, J.-L., V. Monteiller, J. Guilbert, D. Marsan, Y. Cansi, C. Maillard, and J.-P. Santoire (2011), Strain localization and fluid migration from earthquake relocation and seismicity analysis in the western Vosges (France), *Geophys. J. Int.*, doi:10.1111/j.1365-246X.2011.04944.x.

Hardebeck, J. L., and P. M. Shearer (2002), A new method for determining first-motion focal mechanisms, *Bull. Seismol. Soc. Am.*, *92*(6), 2264–2276, doi:10.1785/0120010200.

Heidbach, O., M. Tingay, A. Barth, J. Reinecker, D. Kurfeß, and B. Müller (2008), The World Stress Map database release 2008, doi:10.1594/GFZ. WSM.Rel2008.

Hirn, A., J.-C. Lépine, M. Sapin, and H. Delorme (1991), Episodes of pit-crater collapse documented by seismology at Piton de la Fournaise, *J. Volcanol. Geotherm. Res.*, *47*, 1–2, doi:10.1016/0377-0273(91)90103-7.

Hudson, J. A. (1981), Wave speeds and attenuation of elastic waves in material containing cracks, *Geophys. J. R. Astron. Soc.*, *64*, 133–150.

Husen, S., R. B. Smith, and G. P. Waite (2004), Evidence for gas and magmatic sources beneath the Yellowstone volcanic field from seismic tomographic imaging, *J. Volcanol. Geotherm. Res.*, *131*(3–4), 397–410, doi:10.1016/S0377-0273(03)00416-5.

Johnson, J. H., and M. P. Poland (2013), Seismic detection of increased degassing before Kilauea's 2008 summit explosion, *Nat. Commun.*, *4*(1668), 1–6, doi:10.1038/ncomms2703.

Karalliyadda, S., and M. K. Savage (2013), Seismic anisotropy and lithospheric deformation of the plate-boundary zone in South Island, New Zealand: Inferences from local S-wave splitting, *Geophys. J. Int.*, *193*(2), 507–530, doi:10.1093/gji/ggt022.

Lenat, J. F., and P. Bachelery (1990), Structure and dynamic of the central zone of Piton de la Fournaise volcano, in *Le Volcanisme de la Reunion: Monographie*, edited by J. F. Lenat, Centre de Recherche en Volcanologie, Clermont Ferrand, France.

Li, Y.-G., T. Burdette, J. E. Vidale, K. Aki, and F. Xu (1998), Evidence of shallow fault zone strengthening after the 1992 M7.5, Landers, California, earthquake, *Science*, *279*(5348), 217–219.

Lin, J., and R. S. Stein (2004), Stress triggering in thrust and subduction earthquakes, and stress interaction between the southern San Andreas and nearby thrust and strike-slip faults, *J. Geophys. Res.*, *109*, B02303, doi:10.1029/2003JB002607.

Lomax, A. (2007), The NonLinLoc software guide.

Lomax, A., J. Virieux, P. Volant, and C. Berge (2000), Probabilistic earthquake location in 3D and layered models: Introduction of a Metropolis-Gibbs method and comparison with linear locations, in *Advances in Seismic Event Location*, edited by C. H. Thurber and N. Rabinowit, pp. 101–134, Kluwer Acad., Amsterdam.

Mardia, K. V. (1972), *Statistics of Directional Data*, Academic Press, New York.

Marson-Pidgeon, K., and M. K. Savage (1997), Frequency-dependent anisotropy in Wellington, New Zealand, *Geophys. Res. Lett.*, *24*(24), 3297–3300, doi:10.1029/97GL03274.

Massin, F., V. Ferrazzini, P. Bachèlery, A. Nercessian, Z. Duputel, and T. Staudacher (2011), Structures and evolution of the plumbing system of Piton de la Fournaise volcano inferred from clustering of 2007 eruptive cycle seismicity, *J. Volcanol. Geotherm. Res.*, *202*(1–2), doi:10.1016/j.jvolgeores.2011.01.008.

Matcham, I., M. K. Savage, and K. R. Gledhill (2000), Distribution of seismic anisotropy in the subduction zone beneath the Wellington region, New Zealand, *Geophys. J. Int.*, *140*, 1–10.

Michon, L., A. Di Muro, N. Villeneuve, C. Saint-Marc, P. Fadda, and F. Manta (2013), Explosive activity of the summit cone of Piton de la Fournaise volcano (La Reunion island): a historical and geological review, *J. Volcanol. Geotherm. Res.*, *263*, 117–133.

Nercessian, A., A. Hirn, J.-C. Lepine, and M. Sapin (1996), Internal structure of Piton de la Fournaise volcano from seismic wave propagation and earthquake distribution, *J. Volcanol. Geotherm. Res.*, *70*, 123–143.

Nur, A. (1972), Dilatancy, pore fluids, and premonitory variations of t_S/t_P travel times, *Bull. Seismol. Soc. Am.*, *62*(5), 1217–1222.

Nur, A., and G. Simmons (1969), The effect of saturation on velocity in low porosity rocks, *Earth Planet. Sci. Lett.*, *7*, 183–193.

Peltier, A., P. Bachèlery, and T. Staudacher (2009a), Magma transport and storage at Piton de la Fournaise (La Reunion) between 1972 and 2007: A review of geophysical and geochemical data, *J. Volcanol. Geotherm. Res.*, *184*(1–2), 93–108, doi:10.1016/j.jvolgeores.2008.12.008.

Peltier, A., T. Staudacher, P. Bachèlery, and V. Cayol (2009b), Formation of the April 2007 caldera collapse at Piton de La Fournaise volcano: Insights from GPS data, *J. Volcanol. Geotherm. Res.*, *184*(1–2), 152–163, doi:10.1016/j.jvolgeores.2008.09.009.

Peltier, A., J.-L. Got, N. Villeneuve, P. Boissier, T. Staudacher, V. Ferrazzini, and A. Walpersdorf (2015), Long-term mass transfer at Piton de la Fournaise volcano evidenced 1 by strain distribution derived from GNSS network, *J. Geophys. Res. Solid Earth*, *120*, 1874–1889, doi:10.1002/2014JB011738.

Prôno, E., J. Battaglia, V. Monteiller, J.-L. Got, and V. Ferrazzini (2009), P-wave velocity structure of Piton de la Fournaise volcano deduced from seismic data recorded between 1996 and 1999, *J. Volcanol. Geotherm. Res.*, *184*, 49–62, doi:10.1016/j.jvolgeores.2008.12.009.

Reunion, C. (2008), Manuel d'utilisation du logiciel Circe Reunion v3.2, edited, Institut Geographique National de L'information Geographique et Forestiere, France.

Rivemale, E., F. Brenguier, F. Ferrazzini, V. Battaglia, J. Got, J. Kowalski, P. Nercessian, and B. Taisne (2010), Processes of volcanic unrest inferred from 10 years of micro-seismicity at Piton de la Fournaise volcano, *Eos Trans. AGU, 91*(52), Fall Meet. Suppl., Abstract V32B-06.

Rivet, D., F. Brenguie, D. Clarke, N. M. Shapiro, and A. Peltier (2014), Long-term dynamics of Piton de la Fournaise volcano from 13 years of seismic velocity change measurements and GPS observations, *J. Geophys. Res. Solid Earth*, *119*, 7654–7666, doi:10.1002/2014JB011307.

Roman, D. C., M. K. Savage, R. Arnold, J. L. Latchman, and S. De Angelis (2011), Analysis and forward modeling of seismic anisotropy during the ongoing eruption of the Soufriere Hills Volcano, Montserrat, 1996–2007, *J. Geophys. Res.*, *116*, B03201, doi:10.1029/2010JB007667.

Roult, G., A. Peltier, B. Taisne, T. Staudacher, V. Ferrazini, A. Di Muro, and OVPF team (2012), A new comprehensive classification of the Piton de la Fournaise activity spanning the 1985–2010 period. Search and analysis of short-term precursors from a broadband seismological station, *J. Volcanol. Geotherm. Res.*, *241–242*, 78–104, doi:10.1016/j.jvolgeores.2012.06.012.

Sapin, M., A. Hirn, J.-C. Lepine, and A. Nercessian (1996), Stress, failure and fluid flow deduced from earthquakes accompanying eruptions at Piton de la Fournaise volcano, *J. Volcanol. Geotherm. Res.*, *70*, 145–167.

Savage, M. K. (1999), Seismic anisotropy and mantle deformation: What have we learned from shear wave splitting?, *Rev. Geophys.*, *37*(1), 65–106, doi:10.1029/98RG02075.

Savage, M. K., X. R. Shih, R. P. Meyer, and R. C. Aster (1989), Shear-wave anisotropy of active tectonic regions via automated S-wave polarization analysis, *Tectonophysics*, *165*(1–4), 279–292.

Savage, M. K., A. Wessel, N. A. Teanby, and A. W. Hurst (2010a), Automatic measurement of shear wave splitting and applications to time varying anisotropy at Mount Ruapehu volcano, New Zealand, *J. Geophys. Res.*, *115*, B12321, doi:10.1029/2010JB007722.

Savage, M. K., T. Ohminato, Y. Aoki, H. Tsuji, and S. M. Greve (2010b), Stress magnitude and its temporal variation at Mt. Asama Volcano, Japan, from seismic anisotropy and GPS, *Earth Planet. Sci. Lett.*, *290*(3–4), 403–414, doi:10.1016/j.epsl.2009.12.037.

Schmid, A. (2011), Quelle prédictibilité pour les éruptions volcaniques? De l'échelle mondiale au Piton de la Fournaise, 261 pp, Université de Grenoble, Grenoble.

Schmid, A., J. R. Grasso, D. Clarke, V. Ferrazzini, P. Bachèlery, and T. Staudacher (2012), Eruption forerunners from multiparameter monitoring and application for eruptions time predictability (Piton de la Fournaise), *J. Geophys. Res.*, *117*, B11203, doi:10.1029/2012JB009167.

Shearer, P. M. (2009), *Introduction to Seismology*, Cambridge Univ. Press, Cambridge.

Shudofsky, G. N. (1985), Source mechanisms and focal depth of East African earthquakes using Raleigh wave inversions and body wave modelling, *Geophys. J. R. Astron. Soc.*, *83*, 563–614.

Silver, P. G., and W. W. Chan (1991), Shear wave splitting and subcontinental mantle deformation, *J. Geophys. Res.*, *96*, 16,429–16,454, doi:10.1029/91JB00899.

Silver, P. G., and M. K. Savage (1994), The interpretation of shear-wave splitting parameters in the presence of two anisotropic layers, *Geophys. J. Int.*, *119*(3), 949–963.

Staudacher, T. (2010), Field observations of the 2008 summit eruption at Piton de la Fournaise (Ile de La Reunion) and implications for the 2007 Dolomieu collapse, *J. Volcanol. Geotherm. Res.*, *191*(1–2), 60–68, doi:10.1016/j.jvolgeores.2010.01.012.

Staudacher, T., and A. Peltier (2015), Ground deformation at Piton de la Fournaise (La Reunion Island), a review from 20 years of GNSS monitoring, in *Active Volcanoes of the Southwest Indian Ocean: Piton de la Fournaise and Karthala. Active Volcanoes of the World*, edited by P. Bachelery et al., Springer, Berlin.

Staudacher, T., V. Ferrazzini, A. Peltier, P. Kowalski, P. Boissier, P. Catherine, F. Lauret, and F. Massin (2009), The April 2007 eruption and the Dolomieu crater collapse, two major events at Piton de la Fournaise (La Réunion Island, Indian Ocean), *J. Volcanol. Geotherm. Res.*, *184*, 126–137, doi:10.1016/j.jvolgeores.2008.11.005.

Taisne, B., F. Brenguier, N. M. Shapiro, and V. Ferrazzini (2011), Imaging the dynamics of magma propagation using radiated seismic intensity, *Geophys. Res. Lett.*, *38*, L04304, doi:10.1029/2010GL046068.

Teanby, N. A., J.-M. Kendall, and M. van der Baan (2004), Automation of shear-wave splitting measurements using cluster analysis, *Bull. Seismol. Soc. Am.*, *94*(2), 453–463.

Toda, S., R. Stein, K. Richards-Dinger, and S. Bozkurt (2005), Forecasting the evolution of seismicity in southern California: animations built on earthquake stress transfer, *J. Geophys. Res.*, *110*, B05S16, doi:10.1029/2004JB003415.

Unglert, K., M. K. Savage, N. Fournier, T. Ohkura, and Y. Abe (2011), Shear wave splitting, v(P)/v(S), and GPS during a time of enhanced activity at Aso caldera, Kyushu, *J. Geophys. Res.*, *116*, B11203, doi:10.1029/2011JB008520.

Vanorio, T., J. Virieux, P. Capuano, and G. Russo (2005), Three dimensional seismic tomography from *P* wave and *S* wave microearthquake travel times and rock physics characterization of the Campi Flegrei Caldera, *J. Geophys. Res.*, *110*, B03201, doi:10.1029/2004JB003102.

Volti, T., Y. Kaneda, S. Zatsepin, and S. Crampin (2005), An anomalous spatial pattern of shear-wave splitting observed in Ocean Bottom Seismic data above a subducting seamount in the Nankai Trough, *Geophys. J. Int.*, *163*, 252–264, doi:10.1111/j.1365-246X.2005.02743.x.

Waldhauser, F., and W. L. Ellsworth (2000), A double-difference earthquake location algorithm: Method and application to the Northern Hayward Fault, California, *Bull. Seismol. Soc. Am.*, *90*(6), 1353–1368, doi:10.1785/0120000006.

Walsh, E. (2012), Measuring shear wave splitting using the Silver and Chan method, MS thesis, 157 pp., Victoria Univ. of Wellington, Wellington.

Walsh, E., A. Arnold, and M. K. Savage (2013), Silver and Chan revisited, *J. Geophys. Res. Solid Earth*, *118*, 5500–5515, doi:10.1002/jgrb.50386.

Wang, X.-Q., A. Schubnel, J. Fortin, E. C. David, Y. Guéguen, and H.-K. Ge (2012), High Vp/Vs ratio: Saturated cracks or anisotropy effects?, *Geophys. Res. Lett.*, *39*, L11307, doi:10.1029/2012GL051742.

Zatsepin, S. V., and S. Crampin (1997), Modelling the compliance of crustal rock—I. Response of shear-wave splitting to differential stress, *Geophys. J. Int.*, *129*(3), 477–494.